

Quantum Gravity and Effective Topology

J. van der Duin[†], R. Loll^{†,}, M. Schiffer[†] and A. Silva[†]*

[†] Institute for Mathematics, Astrophysics and Particle Physics, Radboud University
Heyendaalseweg 135, 6525 AJ Nijmegen, The Netherlands.

and

^{*} Perimeter Institute for Theoretical Physics,
31 Caroline St N, Waterloo, Ontario N2L 2Y5, Canada.

Abstract

We introduce a new methodology to characterize properties of quantum spacetime in a strongly quantum-fluctuating regime, using tools from topological data analysis. Starting from a microscopic quantum geometry, generated nonperturbatively in terms of dynamical triangulations (DT), we compute the Betti numbers of a sequence of coarse-grained versions of the geometry as a function of the coarse-graining scale, yielding a characteristic “topological finger print”. We successfully implement this methodology in Lorentzian and Euclidean 2D quantum gravity, defined via lattice quantum gravity based on causal and Euclidean DT, yielding different results. Effective topology also enables us to formulate necessary conditions for the recovery of spacetime symmetries in a classical limit.

1 Lattice quantum gravity and observables

The advent of powerful, quantum field-theoretic lattice methods that take both the dynamical and the Lorentzian nature of four-dimensional spacetime into account makes the challenge of understanding quantum gravity nonperturbatively much more concrete and well defined [1–3]. At an abstract level, the task resembles that of lattice QCD, namely to evaluate the nonperturbative path integral in a suitable scaling limit and for an interesting range of physical scales. The gravitational path integral, also called “sum over histories”, is given by the formal functional integral

$$Z = \int \mathcal{D}[g] e^{iS^{\text{EH}}[g]} \quad (1)$$

over diffeomorphism equivalence classes $[g_{\mu\nu}]$ of spacetime metrics $g_{\mu\nu}$, where

$$S^{\text{EH}}[g] = \frac{1}{16\pi G_N} \int_M d^4x \sqrt{|\det(g)|} (R - 2\Lambda) \quad (2)$$

is the Einstein-Hilbert action with a cosmological term. However, because of the very different field content and symmetry structure of general relativity and nonabelian gauge field theory, the technical requirements of the lattice set-up and the nature of the invariant quantum observables differ substantially.

Modern lattice quantum gravity in terms of causal dynamical triangulations (CDT) comes with a computational framework based on Markov chain Monte Carlo (MCMC) methods, adapted to gravity. It currently allows for the investigation of system sizes of about 10^6 building blocks and for measuring observables in a near-Planckian scale window, a rare asset in quantum gravity. CDT lattice quantum gravity combines three key structural features that have enabled its breakthrough results¹: (i) the use of *dynamical* instead of fixed hypercubic lattices, reflecting the dynamical nature of spacetime geometry, (ii) the *exact* implementation of relabelling symmetry, the lattice analogue of diffeomorphism symmetry, and (iii) the presence of a Wick rotation for curved lattice spacetime configurations, which has no counterpart in the continuum and unlocks the application of MCMC technology.

Being able to evaluate the expectation values

$$\langle \mathcal{O} \rangle = \frac{1}{Z} \int \mathcal{D}[g] \mathcal{O}[g] e^{iS^{\text{EH}}[g]}, \quad (3)$$

of geometric observables \mathcal{O} in the deep UV regime is a game changer for quantum gravity [8]: it enables quantitative reality checks in a realm where, as a rule, classical geometric intuition fails due to the presence of large quantum fluctuations of spacetime itself. Importantly, these fluctuations prevent the existence of structures that could meaningfully serve as (quasi-)classical local reference frames. This also implies that most of the local tensorial constructions of textbook general relativity have no obvious, well-defined quantum counterparts *as a matter of principle*.² Nevertheless, even without a smooth structure, length and volume measurements are still available, and serve as elementary ingredients in the construction of geometric observables. Lastly, the absence of any *a priori preferred* background structure in pure gravity requires observables to be nonlocal, as may be achieved e.g. through spacetime averaging. These characteristics of observables indicate the kind of information one can gain from a fully-fledged quantum gravity theory, and reflect the physical nature of what constitutes “quantum spacetime” in a nonperturbative realm.

¹They include the nonperturbative emergence of a quantum spacetime with de Sitter features [4–6] and the discovery of dynamical dimensional reduction [7], see also [1–3] for reviews.

²This goes beyond the need to regularize and renormalize, which continues to hold, like in nongravitational relativistic quantum field theories.

This sets the stage for the present work, where we elaborate on a new class of observables introduced in [9] as a new tool to characterize the microscopic properties of quantum geometry. Generally speaking, observables have been investigated using CDT lattice methods with two main motivations: firstly, to provide tests of the classical limit, by showing that their eigenvalues on sufficiently large scales are compatible with (semi-)classical expectations. Successful examples are the *shape* of the universe, i.e. its spatial three-volume V_3 as a function of proper time τ , together with its quantum fluctuations $\delta V_3(\tau)$ [5,12], and its average scalar curvature [6], which all turn out to match those of a de Sitter space. A second objective is to uncover new physics, in the form of genuine quantum signatures. The corresponding observables must of course be diffeomorphism-invariant and operationally well defined in the lattice framework, but by virtue of their nonperturbative nature may not relate in any straightforward way to the geometric properties of classical spacetimes. These observables can take the form of scaling exponents, characterizing universal aspects of quantum spacetime in a Planckian regime. An example is the anomalous behaviour of the *spectral dimension*, which in CDT lattice quantum gravity was discovered to be 2 (within error bars) near the Planck scale, instead of the classically expected value of 4, in what has since been conjectured to be a universal property of quantum gravity [13].

In a companion paper [9] we highlight this second motivation, using effective topology as a tool to quantitatively assess the “foaminess” of quantum geometry near the Planck scale, which is often conjectured to be some kind of *quantum spacetime foam* [10]. In the present work, we want to emphasize a motivation that relates to the classical limit, more precisely, the recovery of global, cosmological symmetries. This is particularly suggestive in view of the global de Sitter-like properties that have already been found in four dimensions and the fact that classical de Sitter space has a maximal number of isometries. It is not obvious that symmetries are or should be present in a Planckian regime, or can even be defined there in a operationally meaningful way. One may nevertheless expect that *at a sufficiently coarse-grained scale* some notion of *approximate* symmetry may apply. As discussed in [11] and supported by a proof of principle, this requires the construction of diffeomorphism-invariant measures of homogeneity and isotropy, which is highly nontrivial.

Rather than developing this idea further, we want to point out here that the presence of symmetry, in the sense of an (approximate) invariance under a suitable notion of continuous translation or rotation, needs a suitable carrier space on which such transformations can be defined. This implies that at the coarse-graining scale considered, a quantum spacetime must be sufficiently similar to (a piece of) \mathbb{R}^4 in topological terms, without any topological obstructions in the form of holes, nontrivial connectivity (think wormholes) or parts of spacetime that become effectively disconnected. Investigating the effective topology of quantum geometry, as we will do below, allows us to formulate necessary criteria for being “sufficiently nice” to support notions of symmetry at a given scale. As we will see, already for the two-dimensional toy models of Lorentzian and Euclidean quantum gravity, the outcomes are very different.

The remainder of this paper is organized as follows. We introduce the concept of effective topology in Sec. 2, and explain in Sec. 3 how methods from topological data analysis (TDA) can help in investigating observables related to this concept in the context of lattice quantum gravity based on dynamical triangulations. Sec. 4 contains a detailed description of how one proceeds in the particular case of two dimensions to generate a coarse-grained triangulation whose homology is then measured. This requires several steps: the selection of a coarse-grained vertex sample (Sec. 4.1), the construction of the associated Voronoi decomposition (Sec. 4.2) and subsequently its dual, coarse-grained Delaunay triangulation (Sec. 4.3). In Sec. 5 we describe and discuss the results of numerically measuring the expectation values of the Betti numbers for 2D Lorentzian and 2D Euclidean quantum gravity. Our conclusions and an outlook are contained in Sec. 6. Appendix A contains additional technical details on how to

construct the Voronoi decomposition, and Appendix B describes how to locally adjust Delaunay triangulations to make them amenable to the computational library used to determine the Betti numbers.

2 Introducing effective topology

The key idea behind the new observables is to examine the connectivity properties of the quantum geometry – what we will call its *effective topology* or, more precisely, its *effective homology* – on small scales relative to their total linear extension, as a function of a linear coarse-graining scale δ . Recall that the homology of a topological space keeps track of the number of its “holes” of various dimensions, where the dimension is defined as that of the hole’s boundary.³ For example, removing a two-dimensional disc from a two-dimensional sphere creates a one-dimensional hole, since the hole’s boundary is a one-dimensional circle.

Note that the topology of the spacetime configurations contributing to the lattice path integral is always fixed, usually to that of a sphere or torus, and not allowed to change during the Monte Carlo evolution.⁴ However, due to the nonperturbative character of the gravitational dynamics, typical configurations in the continuum limit are highly nonclassical and nowhere differentiable, analogous to the nonclassical paths that support the Wiener measure of the quantum-mechanical path integral for a nonrelativistic particle. In particular, the microscopic building blocks can arrange themselves into geometries that are macroscopically indistinguishable from spaces with a *different* topology.

An example, in this case involving the global topology of spacetime, has been observed in 4D quantum gravity. The most common choice of lattice topology for this system is $S^1 \times S^3$, where for technical convenience the time direction has been compactified to a circle.⁵ However, it turns out that in the so-called de Sitter phase the overall shape of the quantum geometry (the system’s nonperturbative ground state) is driven dynamically to that of a four-sphere S^4 [4]! More specifically, a typical member of the ensemble of geometries consists of a thin “stalk”, a proper-time interval during which the spatial three-volume $V_3(\tau)$ is close to the kinematically allowed minimum, whose spatial extension is of the order of the UV cut-off a (the length of a lattice edge), and a spherical “blob”, a complementary time interval during which the spatial universe is macroscopically extended, $V_3(\tau) \gg a^3$ (Fig. 1). From a macroscopic point of view (where $a \rightarrow 0$ in a continuum limit) the stalk has vanishing volume and can be neglected relative to the total volume of the blob, leading to an “effective” large-scale topology S^4 .

We will look systematically for the possible presence of nontrivial effective topology at scale δ (with δ assumed small compared to the total system size), as a novel way to characterize the local nature of quantum geometry. Roughly speaking, this is meant to capture the topology “felt” by a probe of linear extension δ or a wavelike excitation of wave length δ , and is related to the presence of holes of characteristic linear size $\leq \delta$. To determine the effective topology in practice, we apply a single coarse-graining step of magnitude δ to a given, typical path integral history.⁶ This operation decimates the number of simplicial building blocks and generates a

³Note that homology is also characterized by torsion coefficients. They are not computed by the open-source library we use, and will not be considered in this work.

⁴The gravitational path integral cannot be renormalized (unambiguously) by standard methods if a sum over topologies is included, due to the superexponential growth of the number of configurations as a function of the spacetime volume (see e.g. [14], Q14, for a discussion). The spaces of fixed topology we consider here are always compact without boundary.

⁵4D CDT has also been investigated on a four-torus T^4 . A discussion of how the choice of global topology may influence the nature of phase transitions can be found in [15].

⁶Recall that the configurations of (C)DT in d dimensions are simplicial manifolds made of d -simplices (a 0-simplex is a vertex, a 1-simplex an edge, a 2-simplex a triangle, a 3-simplex a tetrahedron, etc.) with all edges of identical length, up to an overall multiplicative factor distinguishing space- from time-like link lengths.

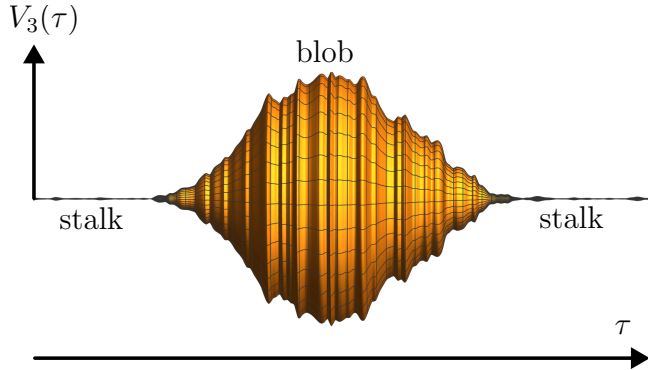


Figure 1: Shape of a typical path integral configuration in 4D CDT lattice quantum gravity, illustrating the macroscopically emergent S^4 -topology. The curve $V_3(\tau)$ has been made into a rotational body about the horizontal time axis τ .

coarse-grained triangulation with edge length $\delta \geq 2$ in lattice units (i.e. setting $a = 1$), for a range of δ .

During the coarse-graining step we monitor for effective topology changes affecting the number of connected components, loops or higher-dimensional voids. For example, the original geometry may contain *necks*, which by definition are closed loops of edge length $\leq \delta$, whose length is minimal with respect to local deformations⁷. After the coarse-graining, these necks will typically be very thin or even pinch to a point, such that the two pieces of geometry on either side of the neck or pinching point can be regarded as effectively disconnected, corresponding to an effective topology change. As another example, consider a Swiss cheese-style quantum geometry. Depending on how the coarse-graining is set up, holes of linear size $\leq \delta$ may disappear in an effective sense at coarse-graining scale δ .

3 Quantum geometry and homology

An attractive feature of this construction is the availability of powerful open-source software to compute the homology of large simplicial complexes, which includes the triangulations that are generated by our coarse-graining procedure. The larger context for these mathematical and numerical techniques is the field of topological data analysis (TDA), whose main objective is to characterize and analyze large sets of data in terms of a basic set of topological and geometrical properties that can be associated with them (see [16, 17] for motivation and introduction).

In a typical application of TDA, the input is a point cloud, i.e. a finite set of data points in a linear space \mathbb{R}^n , which may be of very high dimension, where each pair of data points has a mutual distance induced by the Euclidean metric on \mathbb{R}^n . The point cloud together with this distance matrix is then converted to a triangulated geometric object, more precisely, a simplicial complex [18]. The latter is defined as a set \mathcal{K} of simplices such that any subsimplex (“face”) of an element in \mathcal{K} is again in \mathcal{K} , and the intersection of two elements σ_1, σ_2 of \mathcal{K} is either empty or a subsimplex of both σ_1 and σ_2 . There are several ways of obtaining such a complex, but a standard strategy is to draw balls of radius ϵ around the points in the cloud. Whenever $d + 1$ of these ϵ -balls have a nonempty intersection, the d -simplex spanned by their centre points is added to the simplicial complex, forming a so-called Čech complex. In *persistent homology*, an important methodology in TDA, one studies the homology of the simplicial complexes associated with a given point cloud as a function of the spatial resolution ϵ , and is particularly interested in the topological aspects that are stable as ϵ is varied (see [19]

⁷more precisely, local edge reroutings, since any path has to run along discrete lattice edges

for a concise description).

We borrow some of these ideas and adapt and apply them to the quantum geometries generated in lattice quantum gravity. In the present work, we treat two toy models of quantum gravity in 2D explicitly, providing a proof of principle for the methodology. As far as we are aware, TDA tools have not been applied previously in quantum gravity, with the exception of [20], where they are employed in search of a geometrical spacetime interpretation of certain tensor decomposition data in the context of a canonical tensor model. In terms of ingredients, the present work also has some similarities with [21], which aimed to recover aspects of the homology of continuum spacetime from fundamentally discrete causal sets, invoking simplicial complexes at an intermediate stage of the computation.⁸ In adjacent fields, persistent homology has been applied in string theory to study string compactification spaces and flux vacua (see [22] for a review), and in classical cosmology to describe the large-scale matter distribution of the universe (see e.g. [23] and references therein).

We will compute the expectation values of Betti numbers of coarse-grained quantum geometries as a function of the coarse-graining scale δ , which plays the role of the resolution ϵ mentioned above. The Betti numbers are integers β_k counting the number of k -dimensional holes of a simplicial complex \mathcal{K} or, more formally, measuring the rank of its k th homology group $H_k(\mathcal{K})$ [24].

Our starting point are the triangulated configurations of the gravitational path integral on the lattice, given by what in the literature are variably called piecewise flat, simplicial or combinatorial d -manifolds [1, 25, 26], which in addition to their topological properties also carry metric properties, by virtue of length assignments to the edges of their constituent d -simplices.⁹ By assumption, the interior of each d -simplex is flat, which entails that its metric properties are uniquely determined by its edge lengths. A simplicial manifold satisfies the condition that the *link* of each of its i -simplices, $i \in [0, 1, \dots, d - 1]$ is homeomorphic to the sphere S^{d-i-1} .¹⁰ This is the simplicial analogue of the manifold condition that the neighbourhood of each point is homeomorphic to an open subset of \mathbb{R}^d . From the point of view of the underlying simplicial complex, it implies that every i -simplex is defined *uniquely* by a set of $i + 1$ *distinct* vertices, which is also an input requirement for the “simplex tree” simplicial complex module of the GUDHI library [28] we used to determine the Betti numbers of the coarse-grained triangulations.

4 Coarse-graining triangulations

For a given triangulated configuration T of the gravitational path integral, our coarse-graining procedure at resolution δ consists of three steps: (i) select a subset \mathcal{S}_δ of the set $V(T)$ of all vertices of T , such that the link distance between typical nearest neighbours – the number of edges in the shortest path connecting the two vertices – is of the order δ , (ii) construct the Voronoi cells and Voronoi decomposition of \mathcal{S}_δ , and (iii) construct the dual of the Voronoi decomposition, which is the searched-for coarse-grained Delaunay triangulation, whose Betti numbers are subsequently being determined. To illustrate the procedure and some of the subtleties involved, we will next describe these steps in detail for two-dimensional equilateral triangulations, which feature in the lattice formulations of both Euclidean quantum gravity and causal, Lorentzian quantum gravity after performing the Wick rotation. Elements of

⁸We thank R. Sorkin for bringing this reference to our attention.

⁹Note that for the two-dimensional Euclidean dynamical triangulations considered in Sec. 5.2 below we used a slight generalization of combinatorial manifolds, the *restricted degenerate ensemble* in the classification of [27], where a pair of vertices can be connected by more than one edge.

¹⁰See [26] for a definition of “link” (not to be confused with link in the sense of edge) and further technical details, and [27] for a discussion and illustration of this and other, less stringent, regularity conditions on triangulations that have been used in 2D quantum gravity.

our construction below are similar to a coarse-graining proposed earlier in [29], albeit with a different motivation and application in mind.

4.1 Creating a vertex sample

Our aim is to construct a subset \mathcal{S}_δ of vertices which samples the vertex set $V(T)$ of the triangulation T evenly at a given scale $\delta \in \mathbb{N}$. To achieve this, we use a construction loosely analogous to that of Poisson disk sampling on smooth manifolds [30, 31]. Defining an “open” geodesic ball of radius δ centred at a vertex v by $B_\delta(v) := \{v' \in V(T) | d(v, v') < \delta\}$, where d denotes the (integer-valued) link distance, we will require that (i) $\bigcup_{v \in \mathcal{S}} B_\delta(v) = V(T)$, i.e. each vertex of T lies in at least one δ -ball, and (ii) for any pair $v, v' \in \mathcal{S}_\delta$ with $v \neq v'$, $v' \notin B_\delta(v)$, i.e. no vertex from the sample \mathcal{S}_δ lies in the δ -ball of another sample point, which also implies that $d(v, v') \geq \delta$. In addition, we define the δ -annulus $A_\delta(v)$ of a vertex v as the set $A_\delta(v) := \{v' \in V(T) | \delta \leq d(v, v') < 2\delta\}$.

To generate an evenly distributed vertex sample, we work with three dynamical sets¹¹: the set \mathcal{S}_δ , which at the end of the algorithm will be the searched-for sample set, the set $\mathcal{S}_{new} \subset \mathcal{S}_\delta$, which consists of sampled vertices whose annulus still needs to be explored, and the set $V_{cov} \subset V(T)$ of vertices that have already been covered by geodesic balls.

At the outset, these lists are empty. After picking an initial vertex $v_0 \in V(T)$, the algorithm proceeds as follows:

1. Add v_0 to both \mathcal{S}_δ and \mathcal{S}_{new} as a newly sampled vertex and add all vertices contained in the ball $B_\delta(v_0)$ around v_0 to V_{cov} , implying that those vertices have been covered.
2. Remove a randomly¹² chosen vertex v from \mathcal{S}_{new} and determine its annulus $A_\delta(v)$. Then
 - A. select a random vertex u from $A_\delta(v) \cap (V \setminus V_{cov})$, i.e. the part of the annulus that is not yet covered by geodesic balls;
 - B. add u to both \mathcal{S}_δ and \mathcal{S}_{new} and add all vertices of the δ -ball around u to V_{cov} ;
 - C. if $A_\delta(v) \cap (V \setminus V_{cov})$ is nonempty, repeat from 2a.
3. If \mathcal{S}_{new} is nonempty, repeat from 2.

Fig. 2 is a schematic, planar illustration of elements of this algorithm. Note that we only indicate the vertices that end up in the sample \mathcal{S}_δ (in green), and not any of the other vertices contained in the geodesic δ -balls around them. In Fig. 2d, the combined red region represents the set V_{cov} up to this stage, while the blue region contains the vertices that still need to be covered by the algorithm.

At the end of this process, we have created a vertex sample \mathcal{S}_δ which by construction satisfies condition (ii) from the beginning of Sec. 4.1. To see that it also satisfies (i), we can argue by contradiction. Assume that (i) does not hold and there therefore exists a vertex $w \notin V_{cov}$. This vertex must have a distance of at least 2δ from all elements of \mathcal{S}_δ , since the algorithm by construction covers all vertices inside this radius. Since T by assumption is connected, there is a (possibly nonunique) vertex $p \in \mathcal{S}_\delta$ which has a finite, minimal link distance $d_{min} = d(p, w) \geq 2\delta$ to w . In other words, there is a (possibly nonunique) chain of d_{min} consecutive edges between p and w that form a path of this minimal length. At $2\delta - 1$ steps from p along this chain there is therefore a vertex q , which lies in the annulus $A_\delta(p)$, and has distance $d_{min} - 2\delta + 1$ from w . Although q itself may not be in \mathcal{S}_δ , it must lie in a δ -ball of some other vertex $q' \in \mathcal{S}_\delta \cap A_\delta(p)$, since by construction the annulus $A_\delta(p)$ is completely

¹¹By construction, the algorithm does not add vertices that were already present in \mathcal{S}_δ and \mathcal{S}_{new} ; these sets may be implemented computationally as dynamical arrays. The set V_{cov} can be implemented as a Boolean array.

¹²Here and elsewhere, “random” means according to a uniform distribution over all elements in the set.

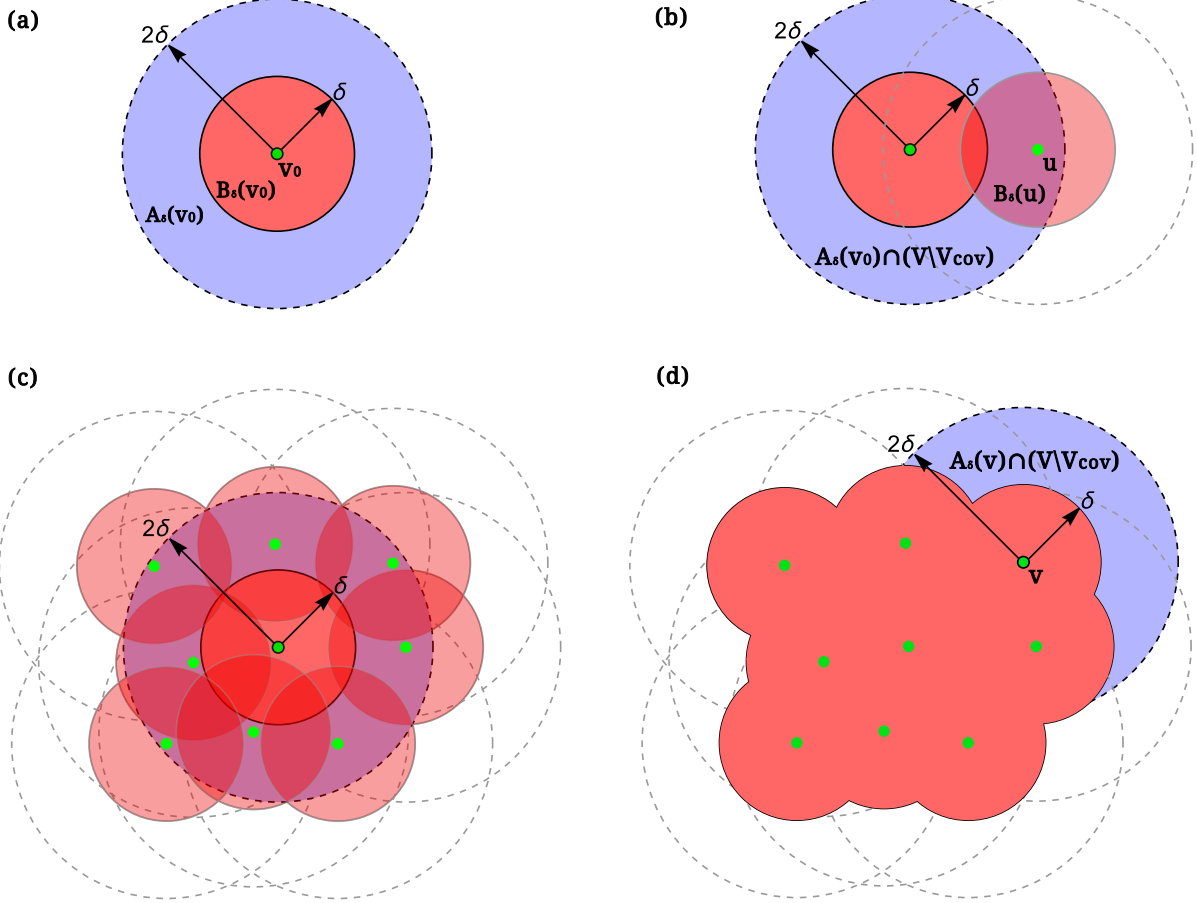


Figure 2: Illustrating the covering algorithm: (a) initial vertex v_0 , together with its δ -ball $B_\delta(v_0)$ (red) and δ -annulus $A_\delta(v_0)$ (blue); (b) random vertex u from the part of the annulus not yet covered, together with its δ -ball $B_\delta(u)$ (pink); (c) after several iterations, all vertices in $A_\delta(v_0)$ have been covered; (d) algorithm continues with a random vertex $v \in \mathcal{S}_{new}$ whose annulus is not yet covered.

covered by δ -balls. From $d(q, q') \leq \delta - 1$ it then follows that $d(q', w) \leq d_{min} - \delta$, which implies that the sample vertex $q' \in \mathcal{S}_\delta$ is closer to w than $p \in \mathcal{S}_\delta$, contradicting our original choice of p . Thus we have shown that condition (i) holds too. To summarize, we have shown that our construction delivers an evenly spread set of sample points.

4.2 Constructing Voronoi cells

Given a sample \mathcal{S}_δ for a given triangulation T , our next step is to partition the set $V(T)$ of all vertices into Voronoi cells, and subsequently extend this to a Voronoi decomposition of the entire two-dimensional triangulation. The Voronoi construction is most familiar as a prescription for decomposing (“tessellating”) the Euclidean plane into n cells associated with a set of seed points $\{p_i, i = 1, 2, \dots, n\}$, where the Voronoi cell associated with a given point p_i is given by the set of all points closer to p_i than to any other point p_j , $j \neq i$, or at an equal distance to such points. An analogous prescription can be used on a graph of the type considered here (see, e.g. [32]): the cell associated with a given vertex $v \in \mathcal{S}_\delta$ will by definition consist of all vertices closer to v (in terms of the link distance) than to any other $v' \in \mathcal{S}_\delta$. If a vertex has the same distance to more than one seed vertex, a random assignment is made, as specified below.

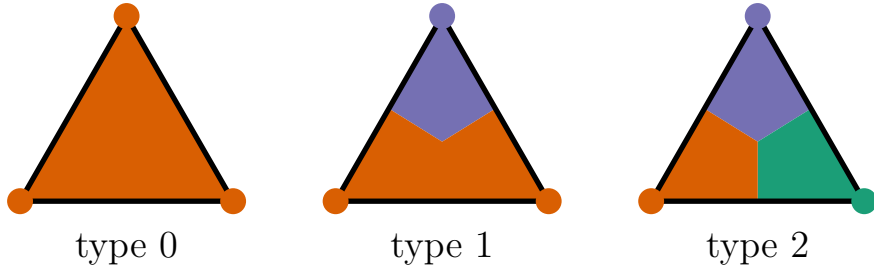


Figure 3: Triangles can have three types of colouring, depending on the colouring of their vertices, generated during the decomposition of vertices into Voronoi cells.

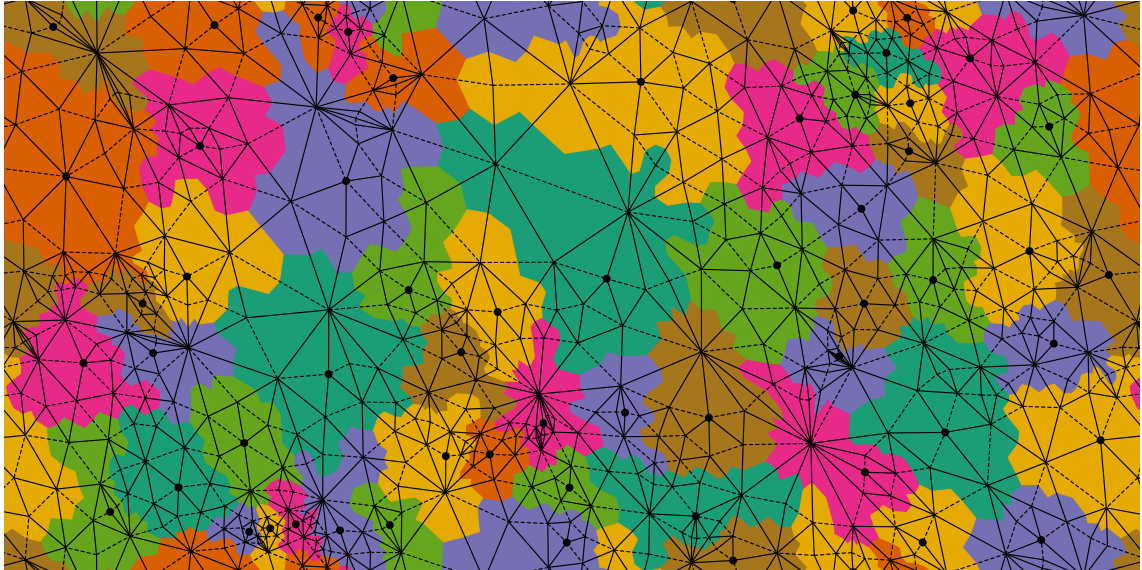


Figure 4: Voronoi decomposition into cells of a 2D CDT configuration on a torus, for $\delta = 3$, using a Tutte or barycentric embedding, where each vertex is located at the barycentre of its neighbours. Dashed and solid lines represent space- and timelike edges respectively, and each black dot is a seed vertex for a cell of a given colour. Note the toroidal periodicity for opposite sides of the rectangle.

Our seed points will be the vertices in S_δ , and the “cell” corresponding to a given seed vertex v is found by performing a breadth-first search of its neighbouring vertices for increasing link distance $d = 1, 2, \dots$ from v . Algorithmically, we perform the breadth-first search radially outward from all seeds simultaneously, in unit steps. This means that at the d th step we assign vertices to the cell of the nearest seed and make a random assignment (with uniform probability) in case there is more than one seed at distance d , before moving on to step $d + 1$. This guarantees that the Voronoi cells defined on the entire triangulation we will construct in the next step are connected.

We now extend the colouring to the triangles of T by dividing each triangle into three “dual” area segments of the same colour as the associated corner vertex. Three types of triangle colouring are possible, depending on whether all three vertices have the same colour (type 0), exactly two vertices have the same colour (type 1), or all three have different colours (type 2), see Fig. 3. For type 1, the triangle contains a boundary between two (two-dimensional) Voronoi cells of different colour, while for type 2 it contains a point where three cells meet, as well as three pairwise boundaries. Fig. 4 shows a typical decomposition of a two-dimensional CDT configuration into such Voronoi cells, where we have associated one cell to each vertex of the evenly distributed sample set S_δ . In this example, each cell has the topology of a disc.

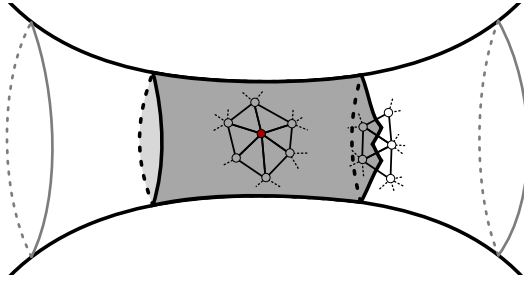


Figure 5: Voronoi cell associated with a seed vertex (in red), with the topology of an annulus (shaded region), wrapping around a thin neck of the triangulation and shown in a three-dimensional embedding.

4.2.1 Properties of Voronoi cells

As illustrated by Figs. 3 and 4, in our construction at most three Voronoi cells can meet in a point. Such a triple point is always located at the centre of a triangle, which can also be viewed as a vertex of the trivalent graph dual to the triangulation T . Likewise, the boundaries between neighbouring cells consist of edges of this dual graph. A sequence of dual boundary edges between two adjacent (along the boundary) triple points we will call a *boundary segment*.

The topology of a typical cell is that of a disc, but any connected subset of the original triangulated manifold can in principle occur. Since we will never consider a cell of maximal volume that covers the entire triangulation, a cell will always have one or more boundaries, each of which is topologically a circle. An important case that appears frequently when coarse-graining 2D Euclidean DT configurations is that of an annulus, i.e. a disc with a hole. This can happen when a cell wraps completely around a “thin neck” of the triangulation, as illustrated by Fig. 5. As we will see in Sec. 4.3.1 below, this is associated with a “pinching” of the coarse-grained triangulation.

Note also that two cells can meet along several, disconnected boundary segments, as illustrated by Fig. 6. This situation can occur when two cells wrap around a thin neck. It can also happen that an entire circular boundary consists of a single boundary segment only, without any triple points, for example, when a disc-shaped cell is surrounded by an annulus.

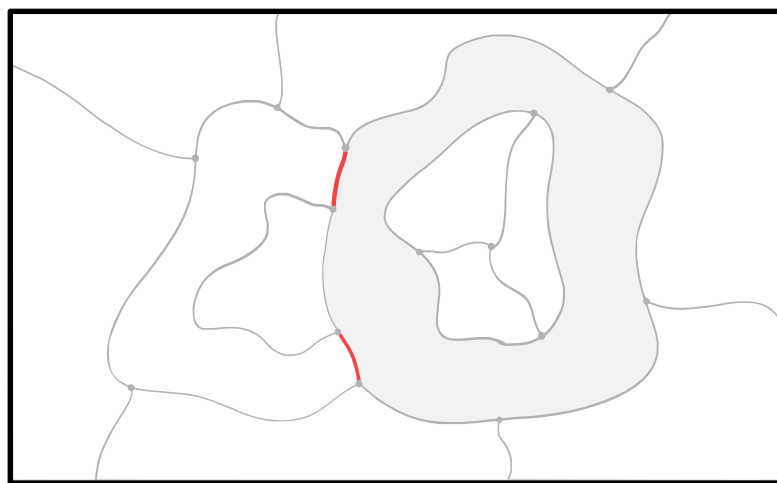


Figure 6: An annulus-shaped (shaded gray) and a disc-shaped Voronoi cell meet along two disconnected boundary segments (in red). This schematic, planar drawing only shows boundary segments and triple points.

4.3 Constructing the dual Delaunay triangulation

Our next objective is to obtain a coarse-grained triangulation T_δ , which is dual to the Voronoi decomposition described in Sec. 4.2, in a sense we will describe below. We are primarily interested in the effective topology of T_δ , where features of up to a linear size δ are “disregarded”. How precisely this is implemented is ultimately a matter of choice. Our general strategy will be to coarse-grain in a way that is maximally topology-preserving, and such that any localized topology changes that occur in this process are well controlled.¹³ This requires a good understanding of the geometric and topological properties of a local neighbourhood of the triangulation, which is rather straightforward in dimension two, but more involved in higher dimensions.

The manner in which we will set up the coarse-graining leads to a slightly generalized notion of “triangulation” for T_δ , compared to the one we started with for T . We will nevertheless call it a *Delaunay triangulation*¹⁴, because it is inspired by a standard construction of the same name in the Euclidean plane (or, more generally, \mathbb{R}^n), with the following properties understood. Firstly, T_δ will in general no longer be a topological manifold, in the sense that it will not look two-dimensional in every point. This happens when thin necks of the original triangulation pinch to a point or collapse to a sequence of one or more edges, which are not part of any triangle. In turn, these edge sequences can also branch into tree-like structures (see also Fig. 11 below). Secondly, even away from points which do not have a \mathbb{R}^2 -like neighbourhood, the two-dimensional triangulation will in general not be a simplicial manifold – according to our definition in Sec. 3 above – because it can happen that two edges share the same endpoints, forming a closed loop of length 2. An explicit example will be presented in Sec. 4.3.1 below.

The coarse-grained Delaunay triangulation T_δ inherits the connectivity properties of its constituent vertices, edges and triangles from the Voronoi decomposition, and is subsequently endowed with metric properties by assigning a uniform length δ to all of its edges and by declaring its edges as straight and its triangles as flat. However, unlike reference [29], we will not be interested in the nontrivial curvature properties of T_δ , but only in its effective topology. The first step to obtaining the Delaunay triangulation identifies subsets of the Voronoi decomposition as dual vertices, edges and triangles, keeping track of their neighbourhood relations:

- (i) with each Voronoi cell we associate a “vertex” inside the cell. This vertex, dual to the Voronoi decomposition, can be thought of as midpoint of the cell, but its actual position is immaterial, since in this step we only keep track of the connectivity of the dual simplicial building blocks of what will become the Delaunay triangulation.
- (ii) With each boundary segment shared by a pair of Voronoi cells we associate an “edge”, whose two endpoints are dual vertices as described in (i). We can construct this dual edge as a simple path that connects the two dual vertices and traverses the boundary segment at some (arbitrarily defined) midpoint. The details of this choice are again unimportant.
- (iii) With each vertex of the Voronoi decomposition we associate a “triangle”, whose edges are the duals to the three boundary segments meeting at the vertex, as described in (ii).

Note that as subsets of the original triangulation T , the “edges” identified in (ii) are in general not straight, and the “triangles” in (iii) are not flat. The searched-for coarse-grained Delaunay triangulation T_δ is now *defined* as the piecewise flat space consisting of the abstract simplicial building blocks identified in steps (i)–(iii), together with their connectivities, where in addition we assign metric properties, namely that all edges are straight and of length δ and all triangles carry a flat Euclidean metric structure induced by their three boundary edges.

¹³Note in particular that for the choice $\delta = 1$ (no coarse-graining) the procedure of Secs. 4.1–4.3 leads to a dual Delaunay triangulation T_1 that reproduces the original triangulation T .

¹⁴also sometimes called a Delaunay complex

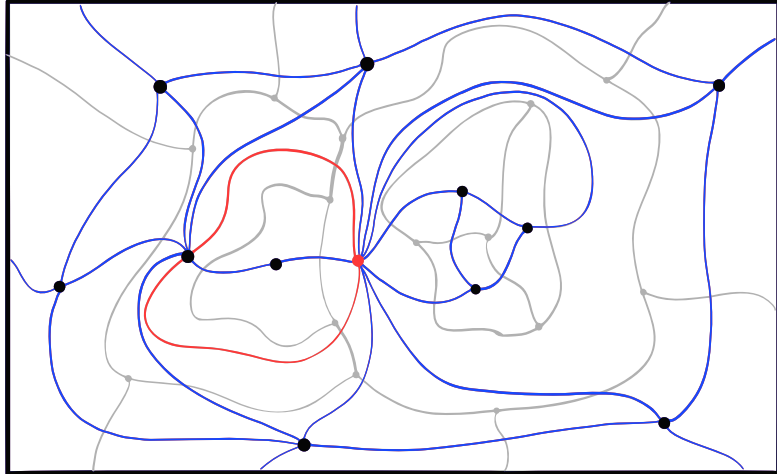


Figure 7: A Voronoi decomposition (black) and its dual Delaunay triangulation (grey). Highlighted in red are a pinching vertex and a closed loop consisting of two edges, dual to the annulus-shaped Voronoi cell and the red boundary segments of Fig. 6 above.

This construction is illustrated by Fig. 7, which shows a piece of a Voronoi decomposition (the same as in Fig. 6 above) and its dual Delaunay triangulation in a schematic, planar representation. The dual vertices at the centre of Voronoi cells and the dual edges, connecting pairs of dual vertices, are drawn in grey. For better readability, we have not coloured the triangles of the Delaunay triangulation, which are dual to trivalent vertices of the Voronoi decomposition and whose boundaries are given by closed loops of three grey edges each.

4.3.1 Properties of the Delaunay triangulation

Fig. 7 also illustrates some of the irregular features of the Delaunay triangulation T_δ we already mentioned above, and which would not occur for a Voronoi decomposition of the Euclidean plane. Firstly, there are the two cells, one with the topology of an annulus, the other one with the topology of a disc, which share two disconnected boundary segments. According to prescription (ii), this leads to two distinct dual edges between the dual vertices associated with these two cells. They form a closed loop consisting of two edges in the Delaunay triangulation, thereby violating the simplicial manifold conditions.

Secondly, the vertex marked in red in Fig. 7, which is dual to the cell with the topology of an annulus, is what we call a pinching vertex. As was already mentioned in Sec. 2, it is associated with the presence of a neck in the original triangulation T , which in the coarse-grained Delaunay triangulation gets pinched down to a point. As a consequence, its neighbourhood is no longer homeomorphic to an open subset of \mathbb{R}^2 , thereby violating the manifold condition.

For our purposes, the most important feature of the coarse-graining process is the pinching that occurs at the location of an annulus. Since the annulus, viewed as a cell of the Voronoi decomposition, by definition does not have any boundary segments in its interior, the dual Delaunay triangulation does not contain any edges that lie entirely inside the annulus. This implies that the coarse-grained triangulation is no longer a two-dimensional manifold at the pinching vertex.¹⁵ Since the annulus separates the Voronoi cells into those lying in- and outside the annulus¹⁶, the resulting Delaunay triangulation will in general have two parts located on

¹⁵For added clarity, one can envisage the pinching as a two-step process: (i) by hand, introduce a single dual edge that links the dual vertex inside the annulus to itself and winds around the annulus once; this preserves the manifold character of the resulting dual triangulation. (ii) Shrink the dual loop of length 1 to a point.

¹⁶This is not necessarily true when T has a global topology with noncontractible loops, but will nevertheless lead to a local pinching.

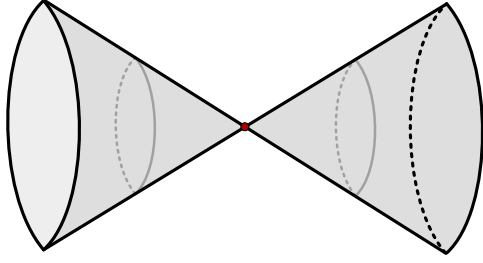


Figure 8: Schematic depiction of a piece of coarse-grained Delaunay triangulation associated with a pinching vertex (red) at which two cones meet. It is dual to the Voronoi cell of Fig. 5, whose seed vertex can be identified with the pinching vertex here.

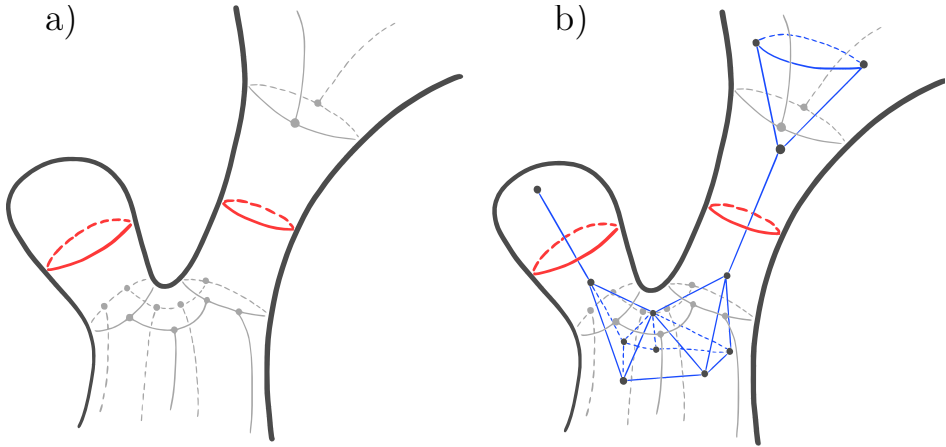


Figure 9: (a): Schematic depiction of a Voronoi decomposition, containing two boundary segments without triple points marked in red. (b): ditto, with the Delaunay triangulation added (blue), containing two loose edges dual to the marked boundary segments.

either side of the pinching vertex, which are connected to each other only at the vertex.

In the simplest case, the neighbourhood of such a pinching point is homeomorphic to that of two two-dimensional cones meeting at their tips (Fig. 8). When the Voronoi cell has the topology of a disc with $h > 1$ holes instead of $h = 1$ (the annulus), the situation generalizes in the simplest case to that of a meeting point of the tips of $h + 1$ cones. Another type of generalization – beyond these simplest cases – occurs when the Voronoi decomposition contains two or more nested annuli. The shared boundary between two such annuli consists of a single boundary segment without any trivalent vertices located on it, which implies that the edge dual to this segment is not part of any triangle in T_δ , but is instead what we will call a “loose” edge. The dual Delaunay triangulation has then not just a pinching vertex, but an entire “pinching edge”, along which the triangulation is locally one-dimensional. This is illustrated by Fig. 9a, which shows two instances of boundary segments without vertices (highlighted in red) of the Voronoi decomposition. The corresponding dual Delaunay triangulation is added in blue in Fig. 9b. The boundary segment between a disc-shaped cap and an annulus on the left branch of the geometry leads in the Delaunay triangulation to a loose edge ending in a single vertex, and the boundary segment between two annuli on the right branch leads to a loose edge connecting two different parts of the coarse-grained Delaunay triangulation.

Yet another irregular feature one can encounter during coarse-graining are so-called “pillows”. By definition, a pillow – in this case of a Delaunay triangulation – consists of two distinct triangles, which share the same three (distinct) vertices and three (distinct) edges.

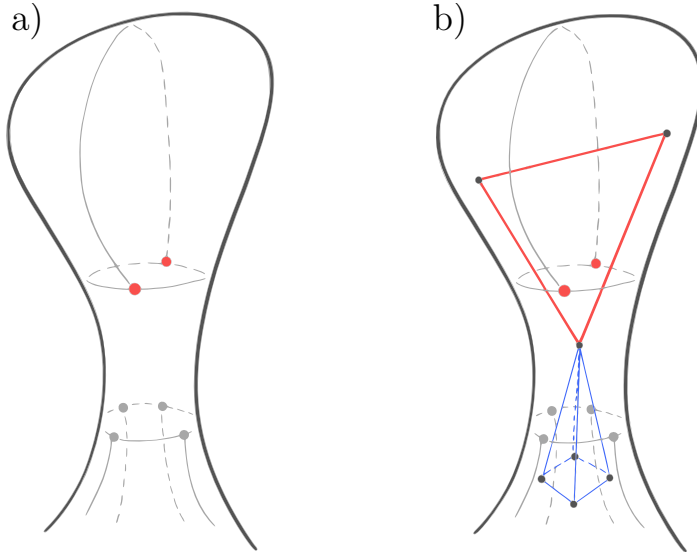


Figure 10: (a): Voronoi decomposition where the same three Voronoi cells are shared by two distinct triple points (red). (b): In the dual Delaunay triangulation, this results in a pillow, consisting of two triangles (red) sharing the same edges and vertices.

This violates the combinatorial character of a simplicial manifold, since the triangles are not uniquely characterized in terms of their vertices. An example of how this can occur is illustrated by Fig. 10. It shows a Voronoi decomposition with the particular property that there are two distinct triple points (marked in red) at which the same three Voronoi cells meet; in the case at hand, these are two discs and one annulus (Fig. 10a). By virtue of our algorithm, this leads to two distinct Delaunay triangles forming a pillow, highlighted in red in Fig. 10b. In the example shown, it is connected to the remainder of the Delaunay triangulation by a pinching vertex, associated with the annulus of the Voronoi decomposition. The occurrence of this type of local structure is relevant for our analysis of the effective topology below, since a pillow is topologically a two-sphere and therefore contributes to the count of the Betti number β_2 .

Note that by construction of the Delaunay triangulations T_δ , no one-dimensional boundaries can appear during coarse-graining, and it also cannot happen that parts of T_δ become disconnected. Consequently, the overall topology of T_δ consists of two-dimensional spherical ‘‘bubbles’’ and generalized bubbles with more complicated shapes¹⁷, connected to each other at pinching vertices or by (sequences of) loose edges, where multiple bubbles and/or loose edges can meet at a given pinching vertex, as illustrated by Fig. 11. The bubbles of minimal size are exactly the pillows we have just introduced.

5 Measuring the effective homology of quantum geometry

In the context of quantum gravity, the effective homology of space(-time) introduced above has the status of a diffeomorphism-invariant observable. In what follows, we will measure this observable with the help of Monte Carlo simulations in two toy models of quantum gravity¹⁸, defined nonperturbatively as continuum limits of gravitational path integrals regularized on dynamical lattices. We will treat the case of Lorentzian quantum gravity, formulated in terms of Causal Dynamical Triangulations (CDT), in Sec. 5.1 and that of Euclidean quantum gravity,

¹⁷e.g. enclosed by surfaces of higher-genus, depending on the topology of the original triangulations T

¹⁸The implementation for both models is open-source [33], with a repository available at <https://gitlab.com/dynamical-triangulation/dyntri-rs>.

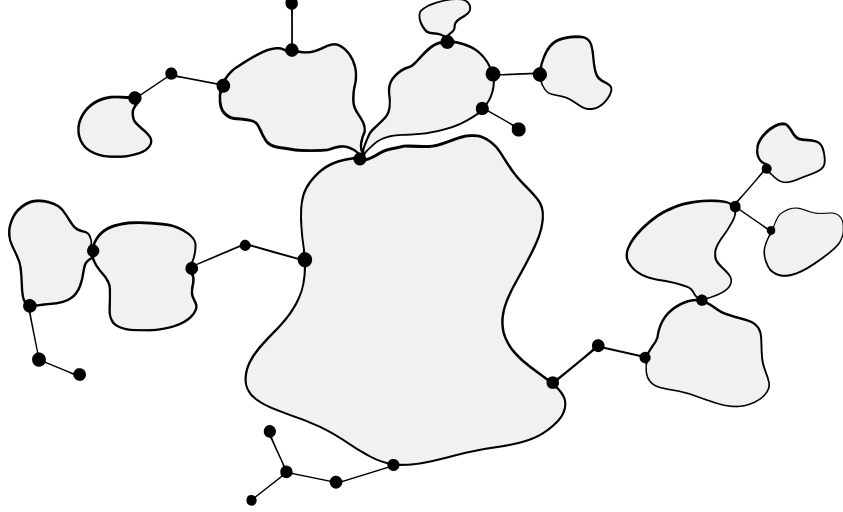


Figure 11: Diagram illustrating the topological features that can occur in a coarse-grained Delaunay triangulation T_δ obtained from a triangulation T of spherical topology. Each circle or “bubble” filled with gray lines represents a spherical triangulation of arbitrary size. Loose edges can connect between such bubbles or be attached to them as outgrowths.

formulated in terms of Euclidean Dynamical Triangulations (EDT), in Sec. 5.2. Among other things, this will help us to assess their suitability as carrier spaces of symmetry.

To set the context, let us recall the computation of Betti numbers of simplicial complexes, which we will use to analyze the Delaunay triangulations produced by the coarse-graining described in Sec. 4 (see e.g. reference [24]). It turns out to be a problem in linear algebra that is amenable to computation and scalable to large triangulations.

The setting is that of a d -dimensional simplicial complex \mathcal{K} , where by definition d is the maximal dimension of any of its simplices. A p -chain c is defined as the formal sum $c = \sum_i a_i \sigma_i^{(p)}$ of p -simplices $\sigma_i^{(p)} \in \mathcal{K}$, where for simplicity we use mod-2 coefficients a_i which can take the values $a_i = 0, 1$. One can also define simplicial homology over larger finite coefficient fields, but for our present purposes this choice will not make a difference.¹⁹ The p -chains form an abelian group $C_p(\mathcal{K})$ under addition. Next, we define a *boundary map* ∂_p , which maps p -chains to $(p-1)$ -chains and on basis elements is defined as

$$\partial_p : C_p \rightarrow C_{p-1}, \quad \sigma^{(p)} = \{v_0, v_1, \dots, v_p\} \mapsto \sum_{i=0}^p \{v_0, \dots, \hat{v}_i, \dots, v_p\}, \quad (4)$$

where we have represented the simplex $\sigma^{(p)}$ by the list of its $(p+1)$ vertices v_i , $\sigma^{(p)} = \{v_0, v_1, \dots, v_p\}$, and the hat denotes the omission of the i th vertex. In geometric terms, eq. (4) says that the boundary of a simplex $\sigma^{(p)}$ is the sum of its $(p-1)$ -dimensional faces. The boundary map allows us to define two subgroups of the group $C_p(\mathcal{K})$ of p -chains, namely (i) the group $Z_p(\mathcal{K})$ of p -cycles c satisfying $\partial_p c = 0$, and (ii) the group $B_p(\mathcal{K})$ of p -boundaries c satisfying $c = \partial_{p+1} d$ for some $(p+1)$ -chain d . It then follows from the fundamental lemma of homology,

$$\partial_p \partial_{p+1} d = 0, \quad \forall d \in C_{p+1}(\mathcal{K}), \quad (5)$$

“the boundary of a boundary is zero”, that the p -boundaries form a subgroup of the p -cycles, i.e. $B_p(\mathcal{K}) \subset Z_p(\mathcal{K})$.

¹⁹In the GUDHI implementation we have used the default field \mathbb{F}_{11} instead of \mathbb{F}_2 .

The p th homology group H_p is then defined as the group of p -chains modulo the group of p -boundaries, $H_p(\mathcal{K}) := Z_p(\mathcal{K})/B_p(\mathcal{K})$. Since all of these groups are also vector spaces, this can be expressed equivalently as the quotient vector space

$$H_p(\mathcal{K}) = \text{kernel}(\partial_p)/\text{image}(\partial_{p+1}). \quad (6)$$

Its dimension,

$$\beta_p(\mathcal{K}) := \dim H_p(\mathcal{K}) = \dim Z_p(\mathcal{K}) - \dim B_p(\mathcal{K}), \quad (7)$$

is called the p th *Betti number*. In other words, the Betti number β_p counts p -cycles that are *not* p -boundaries, which geometrically can be thought of as p -dimensional ‘holes’. In two dimensions, the case at hand, β_0 counts the number of components, β_1 the number of loops (one-dimensional holes), and β_2 the number of two-dimensional holes. We also see that determining the Betti numbers of a simplicial complex involves the computation of the ranks of the linear maps ∂_p .

As already mentioned in Sec. 3, we have used the open-source C++ library GUDHI to compute the Betti numbers of the coarse-grained Delaunay triangulations T_δ . To give an idea of its efficiency, it takes on the order of a second to compute the β_i for a triangulation of size $100k$. However, there is one small step that must still be taken before this library can be used. Implicit in our definition (4) of the boundary map was the unique characterization of each p -simplex $\sigma^{(p)}$ in terms of its $p + 1$ vertex labels. This vertex representation is required by GUDHI as an input format, but is in general not satisfied by our Delaunay triangulations, as we have already seen: the marked, closed loop consisting of two dual edges depicted in Fig. 7 is an explicit example, since both edges share the same vertices. This is merely a technical issue, since the homology of this generalized simplicial complex²⁰ is perfectly well defined. We resolve this by making small local adjustments to the Delaunay triangulation, without changing its homology, such that all of its edges and triangles are uniquely defined through their vertices. Details of this procedure can be found in Appendix B.

5.1 Lorentzian quantum gravity in D=2

We begin by evaluating the expectation values of Betti numbers in coarse-grained spacetimes of resolution δ in two-dimensional Lorentzian quantum gravity. The path integral is given by the two-dimensional analogues of relations (1) and (2), where the integral over the two-dimensional Ricci scalar is a topological invariant and will be dropped from the action. The lattice-regularized version of this path integral is a discrete sum over CDT with a well-defined causal structure. After the Wick rotation it reads [1, 34]

$$Z(\lambda) = \sum_{\text{causal } T} \frac{1}{C(T)} e^{-\lambda N_2(T)}, \quad (8)$$

where λ is the bare cosmological constant, N_2 the number of triangles, and $C(T)$ denotes the order of the automorphism group of the triangulation T , which consists of all maps of T to itself that preserve all of its neighbourhood relations.

Recall that each CDT configuration is a sequence of one-dimensional spatial universes labelled by an integer time $t \in [0, 1, 2, \dots, t_{\text{tot}}]$, where strips assembled from identical, triangular flat building blocks interpolate between adjacent spatial universes of variable size (Fig. 12). This stacked structure of the spacetimes is a lattice implementation of global hyperbolicity, a hallmark of the causal structure of CDT that is not present in the histories of EDT. For convenience we cyclically identify the time direction, $t_{\text{tot}} \equiv 0$, and use compact spatial universes of S^1 -topology, such that all configurations T have the topology of a two-torus $T^2 \equiv S^1 \times S^1$.

²⁰Technically, it is an example of a Δ -complex, which has a well-defined simplicial homology, see [18].



Figure 12: Typical CDT configuration, with volume $N_2 = 4.096$ and time extension $t_{\text{tot}} = 64$, depicting a compact spatial quantum universe whose size fluctuates in time. In the simulations, the time direction is cyclically identified.

The geometric variable characterizing a spatial slice at integer t is its one-dimensional volume, which in lattice units is given by the number $\ell(t)$ of its edges, where we demand $\ell(t) \geq 3$ to ensure that T is a simplicial manifold.

As is customary, our simulations have been performed for ensembles of fixed total volume N_2 , in the present case for eight equally spaced values $N_2 \in [50k, 400k]$. For given N_2 , we have performed measurements for various fixed time extensions t_{tot} . This changes the average spatial volume $\bar{\ell} = N_2/(2t_{\text{tot}})$, which can be interesting to exhibit the dependence of the Betti numbers on global properties of the underlying geometry. Following the considerations of [35], we have used 18 different ratios $r := t_{\text{tot}}^2/N_2$ for each N_2 , evenly spaced in the range $r \in [0.08, 0.25]$. Whenever we study the volume-dependence of a given quantity, we will for simplicity focus on configurations with the intermediate value $r = 0.16$.

The expectation values of geometric observables \mathcal{O} in this ensemble are given by²¹

$$\langle \mathcal{O} \rangle_{N_2} = \frac{1}{\tilde{Z}(N_2)} \sum_{\text{causal } T|_{N_2}} \frac{1}{C(T)} \mathcal{O}(T), \quad \tilde{Z}(N_2) = \sum_{\text{causal } T|_{N_2}} \frac{1}{C(T)}, \quad (9)$$

where the sums are over CDT configurations of fixed volume N_2 and time extension t_{tot} . The fixed-volume path integral $\tilde{Z}(N_2)$ is related to the path integral (8) for fixed cosmological constant by a Laplace transform,

$$Z(\lambda) = \sum_{N_2} e^{-\lambda N_2} \tilde{Z}(N_2). \quad (10)$$

We use a Monte Carlo Markov chain (MCMC) algorithm²² to generate sequences of independent CDT configurations, which allows us to approximate the expectation values $\langle \beta_i \rangle$ of the Betti numbers as the lattice volume is increased systematically. The typical number of measurements ranged from around $410k$ for the smallest volume $N_2 = 50k$ to around $40k$ for the largest volume $N_2 = 400k$.²³ We perform 200 sweeps between measurements, where each sweep consists of

²¹In the remainder of the paper, we will drop the subscript N_2 for notational convenience, but it should be understood that all expectation values refer to constant-volume ensembles.

²²For details on implementing MCMC for two-dimensional CDT, see e.g. [33, 36].

²³For the intermediate volumes $N_2 = 100k, 150k, 200k, 250k, 300k$ and $350k$, the typical number of measurements was on the order of $125k, 65k, 70k, 45k, 60k$ and $55k$ respectively.

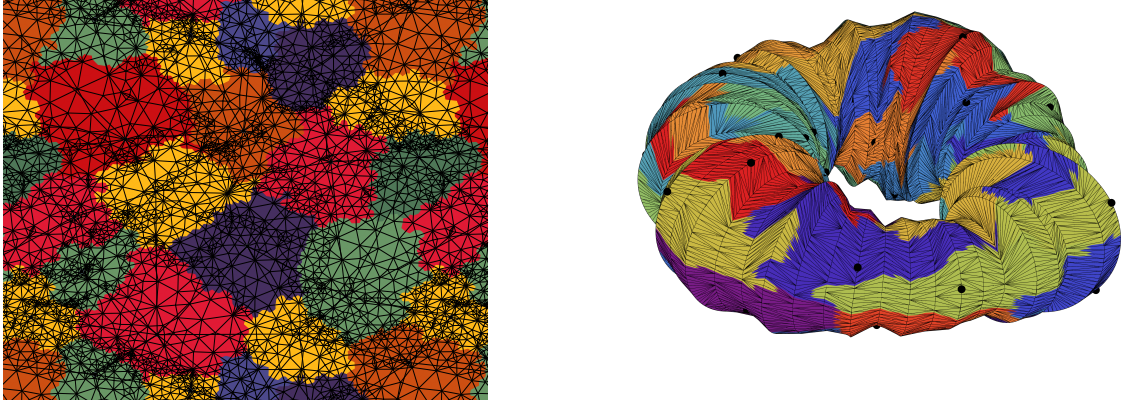


Figure 13: Voronoi decompositions of typical CDT configurations on a two-torus at resolution scale $\delta = 8$, in a planar representation with $N_2 = 5.040$ and $t_{\text{tot}} = 35$ (left), and an embedding in \mathbb{R}^3 with $N_2 = 10.000$ and $t_{\text{tot}} = 52$ (right). Thin black lines are those of the original triangulation T . In the figure on the left, the edges of the dual Delaunay triangulation T_δ have been added as thick black lines.

N_2 attempted Monte Carlo moves. Given the relatively high acceptance rate achieved in our simulations, this means that on average several Pachner moves are performed per simplex. We can therefore safely assume that our measurements are uncorrelated.

Fig. 13 illustrates the nature of typical CDT configurations with their coloured Voronoi cells after coarse-graining with resolution $\delta = 8$, in a planar representation analogous to Fig. 4 (left), and superimposed on the original torus in a three-dimensional embedding (right). Each cell is associated with a vertex from the evenly spread sample \mathcal{S}_8 (indicated by a fat black dot), whose creation was described in Sec. 4.1. Although the original triangulation T – still visible in both representations – is locally curved, the coarse-graining procedure contains random elements, and the representations are not strictly isometric, the resulting patterns of Voronoi cells are still fairly regular. All depicted cells have disc topology and a roundish shape, unlike what we will meet in Euclidean quantum gravity in Sec. 5.2 below.

For a more detailed understanding of our coarse-graining procedure, we have monitored the volumes of the Voronoi cells at resolution δ in terms of the numbers of vertices of the triangulation T they contain. As can be seen from Fig. 14, our algorithm has the property of creating cells of approximately equal size, with volume distributions that remain well peaked even for $\delta > 2$. Across a range of volumes N_2 and time extensions t_{tot} we have investigated, these distributions are essentially unchanged.

We now turn our attention to the expectation values $\langle \beta_i(\delta) \rangle$ of the Betti numbers. Fig. 15 shows the measurement results for the CDT ensemble with volume $N_2 = 200k$ and time extension $t_{\text{tot}} = 179$, in the range $\delta \in [2, 82]$. The original triangulations T , which correspond to $\delta = 1$, i.e. the case without any coarse-graining, by construction have the topology of a torus, with $\beta_0 = 1$ counting its single connected component, $\beta_1 = 2$ the loops along the two directions of the torus, and $\beta_2 = 1$ the single two-dimensional hole or “cavity” enclosed by the torus. We see that throughout most or all of the observed δ -range, the expectation values for the coarse-grained geometries T_δ reproduce these values within error bars. In other words, the effective homology coincides with the original homology even for very large coarse-graining and in this sense does not reveal any new local structure.

Only when the resolution δ reaches a scale where the nontrivial global topology of the torus geometries comes into play, the average Betti numbers $\langle \beta_1 \rangle$ and $\langle \beta_2 \rangle$ can be affected.

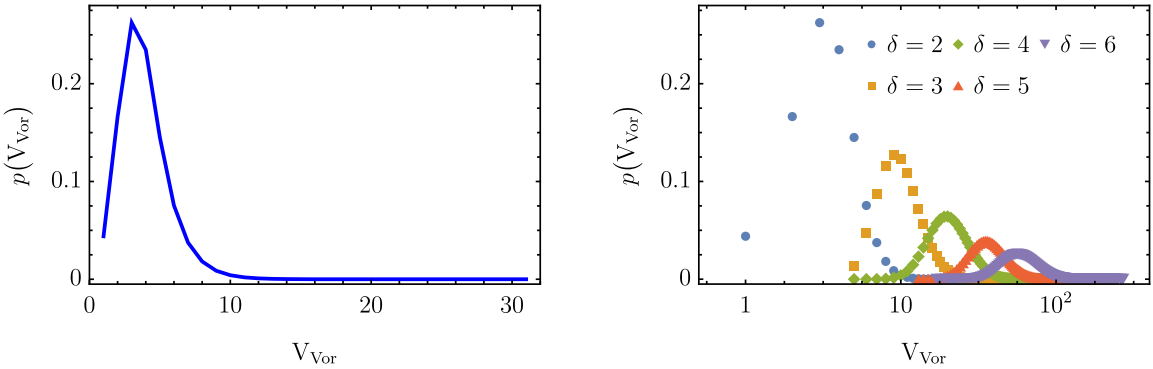


Figure 14: Normalized distribution $p(V_{\text{Vor}})$ of the volume V_{Vor} of individual Voronoi cells in units of vertices of the original triangulation T for CDT configurations of volume $N_2 = 200k$ and time extension $t_{\text{tot}} = 179$, for $\delta = 2$ (left) and for the range $\delta \in [2, 6]$ (right). In this and other data plots below, the size of error bars is smaller than the dot size.

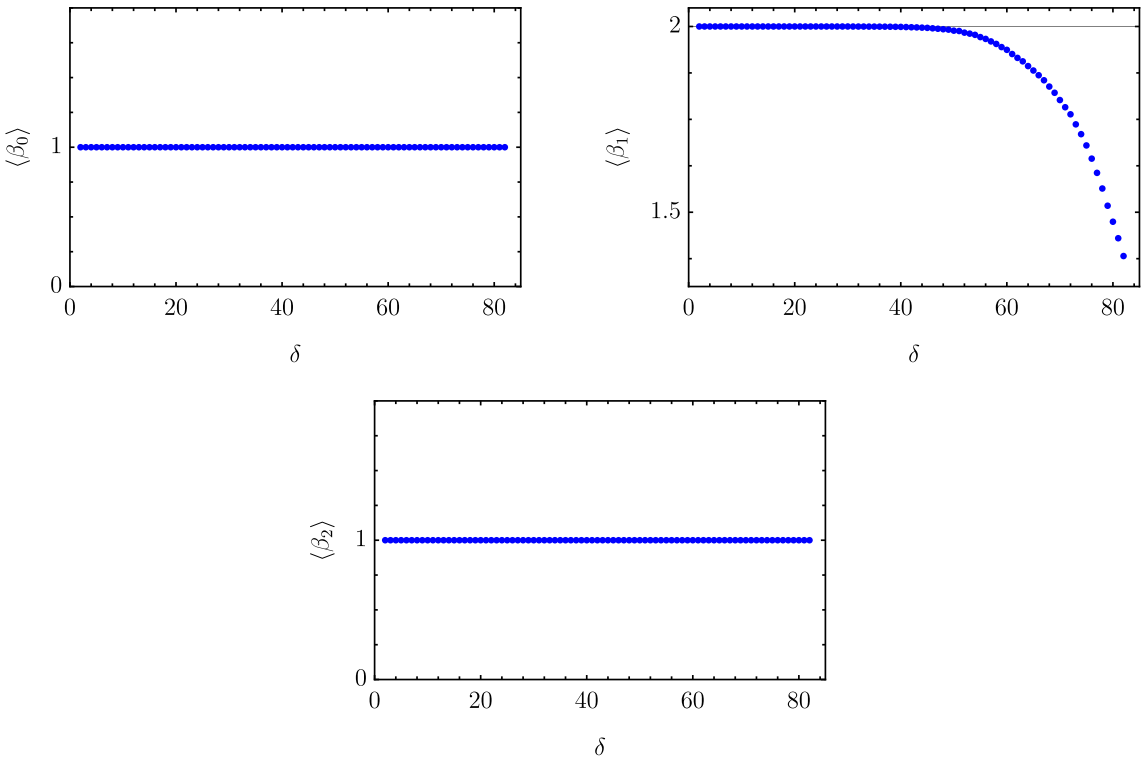


Figure 15: Expectation values of the Betti numbers β_0 , β_1 and β_2 in 2D Lorentzian quantum gravity with $N_2 = 200k$ and $t_{\text{tot}} = 179$, as a function of the resolution $\delta \in [2, 82]$. The straight line at $\langle \beta_1 \rangle = 2$ is included for comparison.

This happens because the diameter of a Voronoi cell can become large enough to wrap around one or both of the compact torus directions. This results in global pinchings of the geometry as described in Sec. 4.3, where the pinchings now take place at noncontractible loops of the original triangulation. By contrast, the expectation value $\langle \beta_0 \rangle$ cannot be affected, since by construction no part of the Delaunay triangulation detaches during a pinching.

The onset of these global features in the behaviour of the Betti numbers depends both on the time extension t_{tot} and the spatial extension of the toroidal configurations. Because the

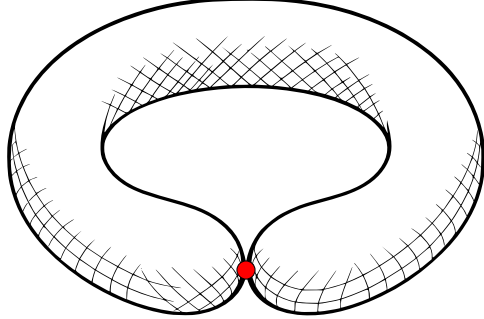


Figure 16: The presence of a single global pinching vertex (red) lowers the Betti number β_1 of a toroidal Delaunay triangulation to 1.

size $\ell(t)$ of the spatial universe is subject to large quantum fluctuations (cf. Fig. 12), the global effect on observables of wrapping around the compact spatial direction becomes noticeable on length scales much smaller than the average spatial extension $\bar{\ell}$, as has been observed in previous studies of other observables in 2D CDT quantum gravity [35, 37]. This is also what we have found in the present study.

For the parameter choices $N_2 = 200k$ and $t_{\text{tot}} = 179$ of the data plots shown in Fig. 15, a nontrivial wrapping of Voronoi cells in the time direction cannot occur, since the maximal diameter of such a cell is of the order of 2δ , which in the δ -range probed is always smaller than t_{tot} . It implies that the deviation from constancy in $\langle \beta_1 \rangle$ for $\delta \gtrsim 38$ observed in Fig. 15 is due to nontrivial global effects in the spatial direction. The leading contribution to the decrease of this expectation value is from configurations with a single global pinching vertex associated with contracting a spatial loop of winding number 1. Namely, for a given Delaunay triangulation T_δ , β_1 drops from 2 to 1 in the presence of a single global pinching, since one of the noncontractible loops of the torus disappears, while β_2 remains unaffected, since there still is a two-dimensional cavity present. This is illustrated schematically by Fig. 16.

There are additional, smaller effects related to multiple pinchings, all of which occur with higher frequency as δ grows. For example, introducing a second pinching vertex in the configuration of Fig. 16, associated with the same direction but in a different location along the torus, will result in the appearance of two spherical cavities or ‘‘bubbles’’, with associated Betti number $\beta_2 = 2$. Correspondingly, additional pinchings can increase the number of bubbles and therefore β_2 even further. All of these lead to an increase in $\langle \beta_2 \rangle$ as δ becomes larger. However, in the measurement of $\langle \beta_2 \rangle$ reported in Fig. 15 their occurrence is so rare that it does not lead to any appreciable deviation from constancy in the entire δ -range considered.

To study these effects more systematically, we have performed series of measurements of the Betti numbers at fixed volume $N_2 = 200k$, where in addition to δ we also vary the time extension, in the range $t_{\text{tot}} \in [126, 224]$, see Fig. 17. Note that for a given triangulation T , whenever the resulting Delaunay triangulation no longer contains any triangles we stop the coarse-graining and discard this configuration, independent of the values of its Betti numbers. It implies that the number of measurements we average over varies as a function of δ . We stop plotting a curve for given t_{tot} when more than 5% of measurements are discarded this way. We have verified on a test sample that this procedure captures the properties of the coarse-grained triangulations correctly, while allowing us to access sufficiently large δ to exhibit the nontrivial behaviour of the Betti numbers.

The expectation value of β_0 , shown in Fig. 17, remains at the constant value 1 throughout, as anticipated. The location of the characteristic drop of the expectation value $\langle \beta_1(\delta) \rangle$ turns out to depend on the time extension t_{tot} . For small t_{tot} , it is primarily caused by pinchings along

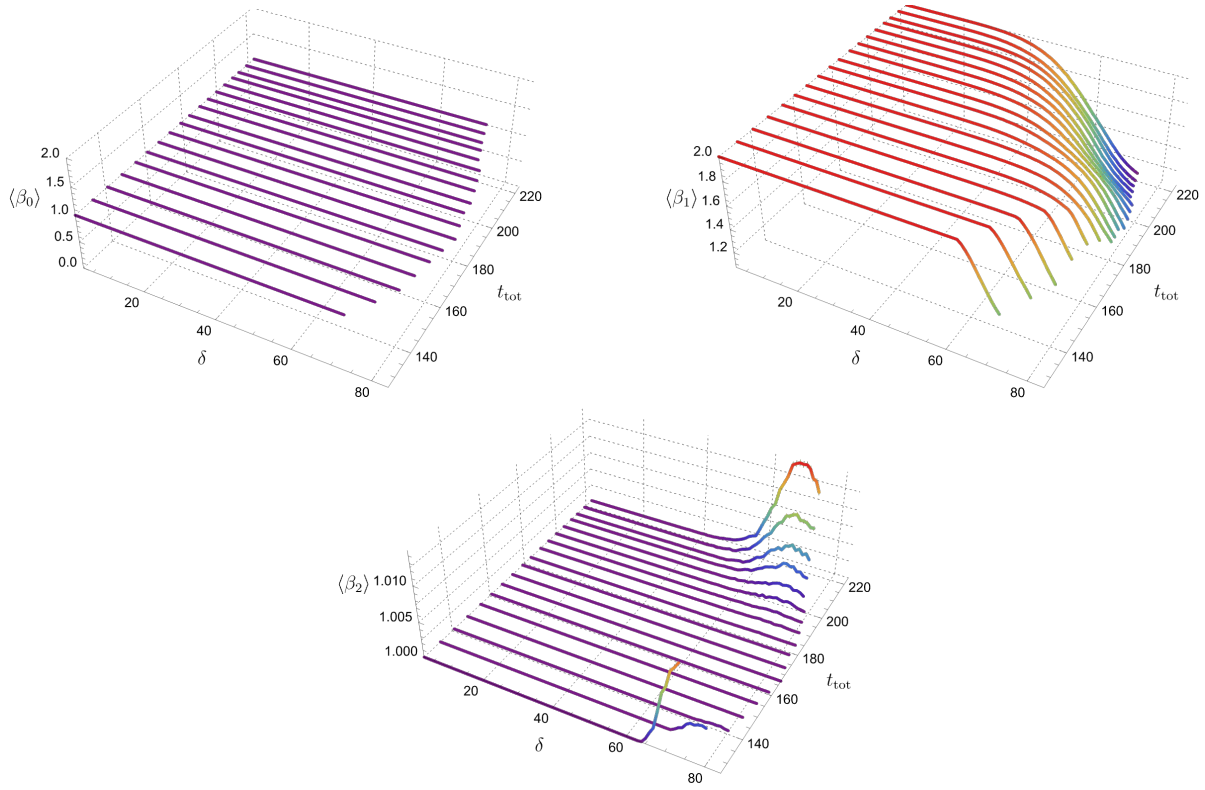


Figure 17: Expectation values of the Betti numbers β_0 , β_1 and β_2 in 2D Lorentzian quantum gravity with $N_2 = 200k$, as a function of the resolution δ and the time extension t_{tot} .

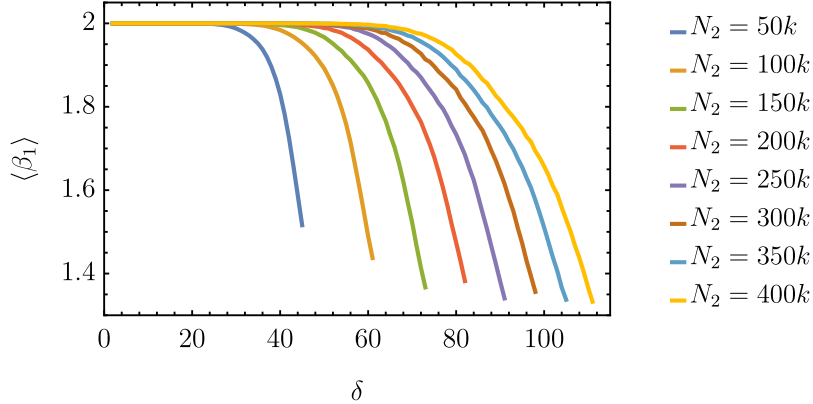


Figure 18: Expectation value $\langle \beta_1 \rangle$ of the first Betti number in 2D Lorentzian quantum gravity as a function of the volume N_2 , for a fixed ratio $r = 0.16$.

the time direction; these become rarer for increasing time extension, pushing the drop-off to larger values of δ . Since a bigger t_{tot} at constant two-volume implies a smaller spatial extension, pinchings along the spatial direction start appearing, leading to a monotonic decrease in the location of the drop-off beyond $t_{\text{tot}} \approx 155$. A complementary set of measurements of $\langle \beta_1 \rangle$, for increasing volume but a fixed ratio r of the time and spatial extensions is given in Fig. 18. Again we observe that the δ -interval where the expectation value is compatible with 2 grows as the volume becomes larger, roughly speaking $\propto \sqrt{N_2}$, as we have checked. The chosen ratio $r = 0.16$ is such that the effect comes from global pinchings of the spatial direction only. Lastly,

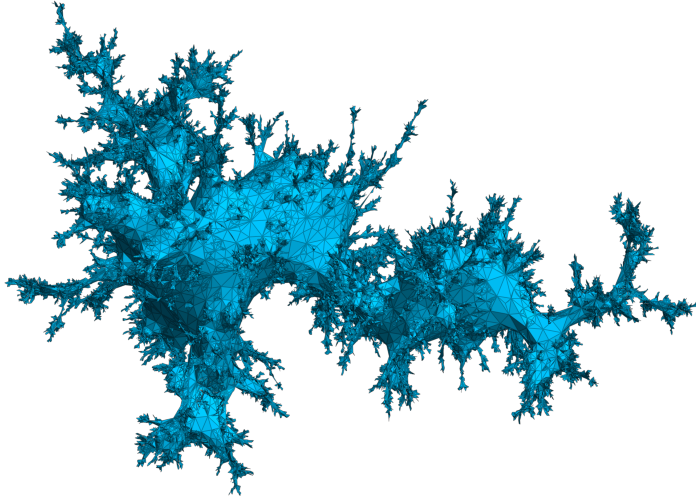


Figure 19: Typical EDT configuration, with volume $N_2 = 100k$, depicting a Euclidean “space-time” of spherical topology.

as explained above, the Betti number β_2 is sensitive to the occurrence of multiple pinchings. Such pinchings along the time direction are in evidence in the measurements of its expectation value for small $t_{\text{tot}} \lesssim 148$ and large δ , while the effects of multiple pinchings along the spatial direction start showing up in the plots for the largest time extensions $t_{\text{tot}} \gtrsim 200$ considered. Note that the absolute size of the change in $\langle \beta_2(\delta) \rangle$ away from the classical torus value is about two orders of magnitude smaller than that of $\langle \beta_1(\delta) \rangle$.

5.2 Euclidean quantum gravity in D=2

We turn next to the analysis of Euclidean quantum gravity in two dimensions. This toy model of quantum gravity is known to lie in a different universality class from the Lorentzian model considered in Sec. 5.1. The crucial difference is the absence of a causal structure for the histories that are summed over in the regularized Euclidean path integral

$$Z^{\text{eu}}(\lambda) = \sum_T \frac{1}{C(T)} e^{-\lambda N_2(T)}, \quad (11)$$

which otherwise is completely analogous to the Wick-rotated path integral (8) of the Lorentzian theory. As already mentioned in footnote 9, the sum is taken over EDT that are elements of a slightly generalized ensemble, compared to that of simplicial manifolds, which is known to not affect the continuum limit of the model. With these specifications observed, each triangulation T in the sum is an arbitrary gluing of flat, equilateral triangles with the topology S^2 of a two-sphere. A typical EDT configuration is shown in Fig. 19, illustrating the well-known fractal nature of its quantum geometry.

We have again computed the expectation values of the Betti numbers, using the analogue of expression (9) for the Euclidean fixed-volume ensemble, for eight equally spaced values $N_2 \in [50k, 400k]$. For each volume, we have performed several hundred thousand measurements on independent configurations.²⁴ The EDT configurations are generated by a direct Monte Carlo sampling method, where each sampled configuration is automatically independent.²⁵

²⁴For the volumes $N_2 = 50k, 100k, 150k, 200k, 250k, 300k, 350k$ and $400k$ we used $344k, 322k, 568k, 552k, 489k, 516k, 440k$ and $459k$ configurations.

²⁵The direct sampling uses a bijection between tadpole-free triangulations and random Kreweras excursions [38], which can easily be sampled directly. The implementation is available at [33].

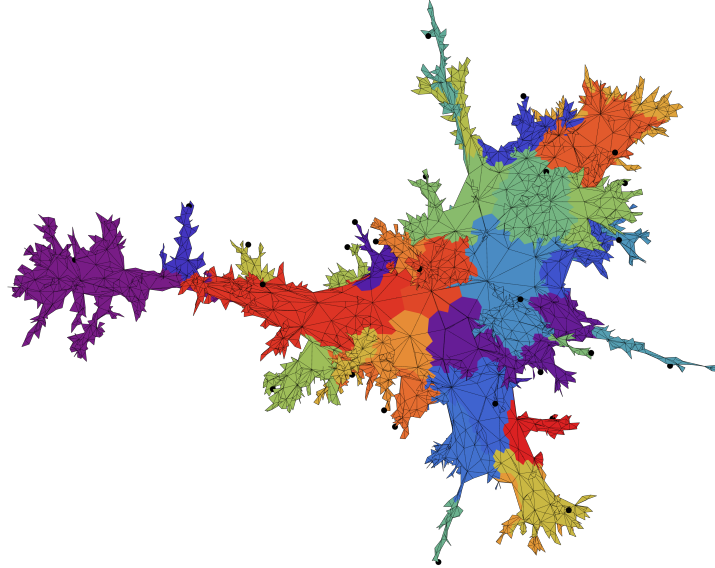


Figure 20: Voronoi decomposition of a typical EDT configuration on a two-sphere at resolution scale $\delta = 8$, with $N_2 = 10k$. Thin black lines are those of the original triangulation T .

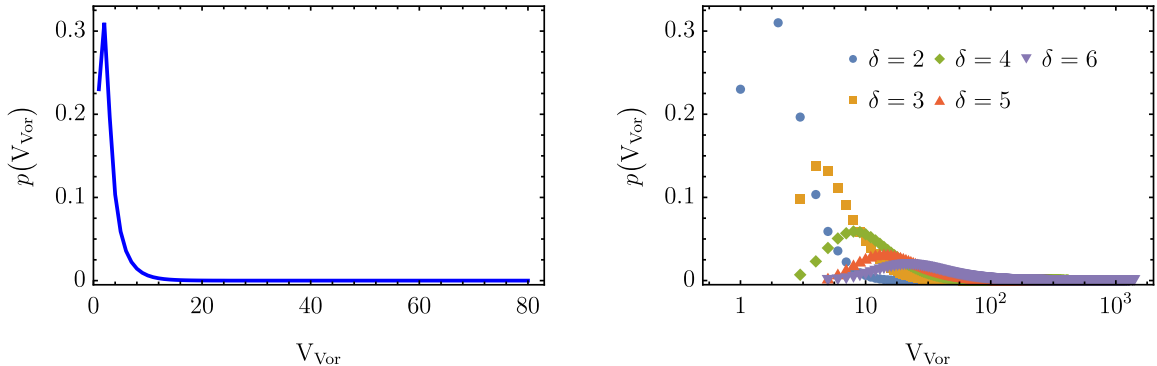


Figure 21: Normalized distribution $p(V_{\text{Vor}})$ of the volume V_{Vor} of individual Voronoi cells in units of vertices of the original triangulation T for EDT configurations of volume $N_2 = 200k$, for $\delta = 2$ (left) and for the range $\delta \in [2, 6]$ (right).

Fig. 20 shows a typical EDT configuration with coloured Voronoi cells after coarse-graining with resolution $\delta = 8$. Each cell is associated with a vertex from the evenly spread sample S_8 (indicated by a fat black dot). Due to the fractal and “spiky” nature of the original triangulation T , the shapes of the cells are much less regular than in the Lorentzian case. Note also that the annuli discussed in Sec. 4.3 are present whenever a Voronoi cell of one colour wraps around an outgrowth that continues with a cell of another colour.

We have checked that our algorithm nevertheless distributes volume among the cells relatively evenly. This is illustrated by Fig. 21, which is the Euclidean analogue of Fig. 14 above, showing the distribution of volumes of the Voronoi cells at resolution δ in terms of the numbers of vertices of the triangulation T . The situation is qualitatively similar to that of the Lorentzian case, with the peaks of the distributions located at slightly lower values of the cell volume V_{Vor} , and somewhat broader distributions for the larger δ -values.

The measurements of the expectation value of the Betti numbers for the EDT ensemble with volume $N_2 = 200k$ in the range $\delta \in [2, 53]$ are displayed in Fig. 22. Before coarse-graining, the triangulations T have the topology of a sphere, with $\beta_0 = 1$ counting its single connected

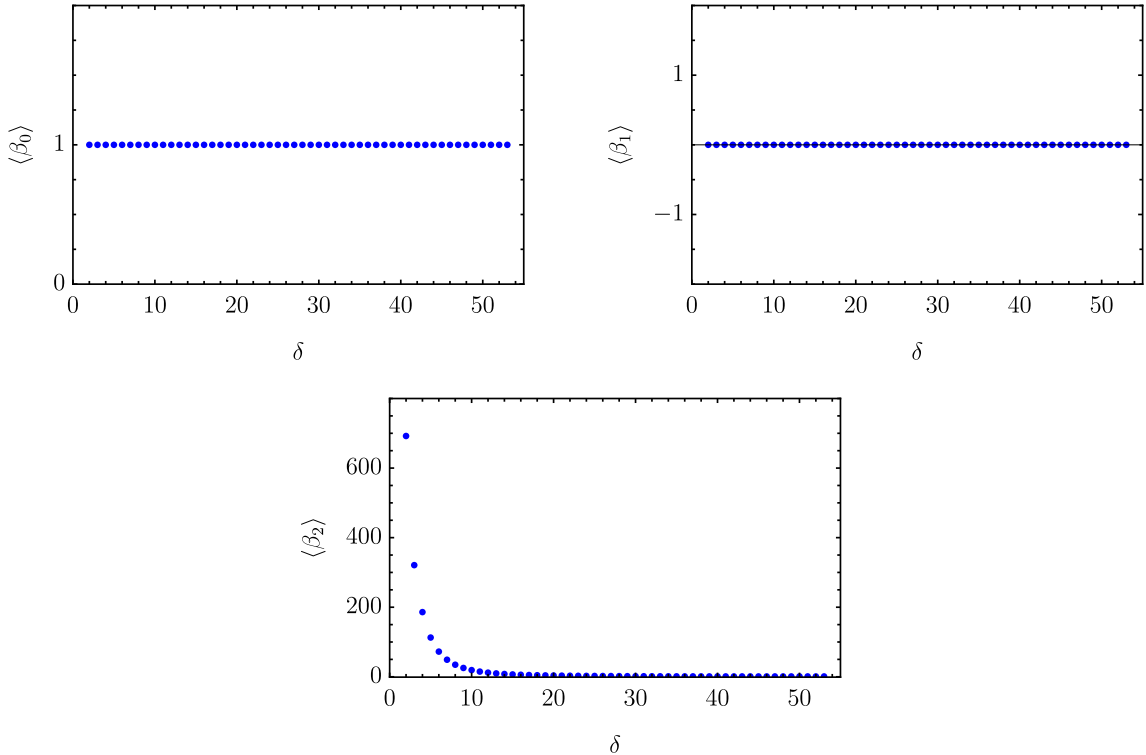


Figure 22: Expectation values of the Betti numbers β_0 , β_1 and β_2 in 2D Euclidean quantum gravity with $N_2 = 200k$, as a function of the resolution $\delta \in [2, 53]$.

component, $\beta_1 = 0$ reflecting the absence of noncontractible loops, and $\beta_2 = 1$ for the single two-dimensional hole enclosed by the sphere. Throughout the entire observed δ -range, not only the expectation values $\langle \beta_0 \rangle$ and $\langle \beta_1 \rangle$ but the Betti numbers β_0 and β_1 for each individual coarse-grained geometry reproduce these values. The constancy of β_0 is unsurprising, since the algorithm we use preserves the connected character of the geometries. In the present case, since the geometries remain also simply connected, this also explains the constancy of β_1 . However, pinchings can in principle happen, where the sphere after coarse-graining becomes a set of connected spherical bubbles, like the structure sketched in Fig. 11 above. This changes β_2 , which counts the number of such bubbles.

The bottom plot of Fig. 22 for the expectation value of β_2 indicates that this is exactly what happens here and, unlike in the Lorentzian case, is a *local* phenomenon. Already for the smallest coarse-graining step $\delta = 2$, the expectation value of β_2 shoots up to a maximum, then decreases steeply as the resolution becomes larger, and asymptotes to 1 for the largest δ -values considered.²⁶ A similar behaviour can be observed for a range of volumes $N_2 \in [50k, 400k]$, where correspondingly more bubbles appear, as shown in Fig. 23, left. The locality of this “bubble generation” is underscored by the fact that for $\delta = 2$, for which we have the best bubble statistics, the average Betti number $\langle \beta_2 \rangle$ for large N_2 scales approximately linearly with the volume, as illustrated by Fig. 23, right.

The generation of these spherical bubbles is illustrated further by the sequence of Delaunay triangulations T_δ , for $\delta = 2, 4, 6$ and 8 , depicted in Fig. 24, which are coarse-grained versions of the triangulation of Fig. 19. At every iteration there is a “mother universe”, drawn in white, which contains most of the volume, and smaller, coloured outgrowths or bubbles that are connected to the mother universe or to other bubbles by pinchings or loose edges. To convey

²⁶Since we do not include configurations where all triangles have vanished, we always have $\beta_2 \geq 1$.

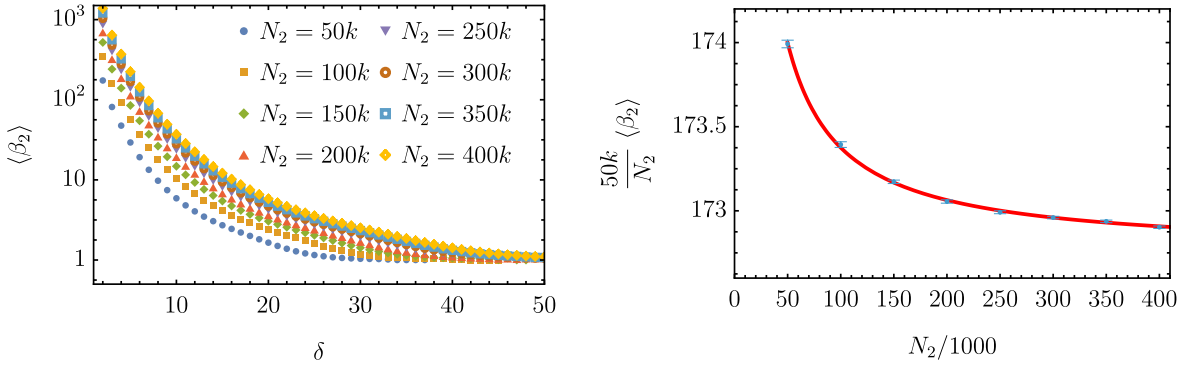


Figure 23: Expectation value of the Betti number β_2 in 2D Euclidean quantum gravity as a function of the resolution δ , for volumes $N_2 \in [50k, 400k]$ (left). The same expectation value, for $\delta = 2$, rescaled by the volume, and plotted as a function of the volume N_2 . The red line is the best fit to $\frac{50k}{N_2} \langle \beta_2 \rangle = A + B/N_2$, for fitting constants A and B (right).

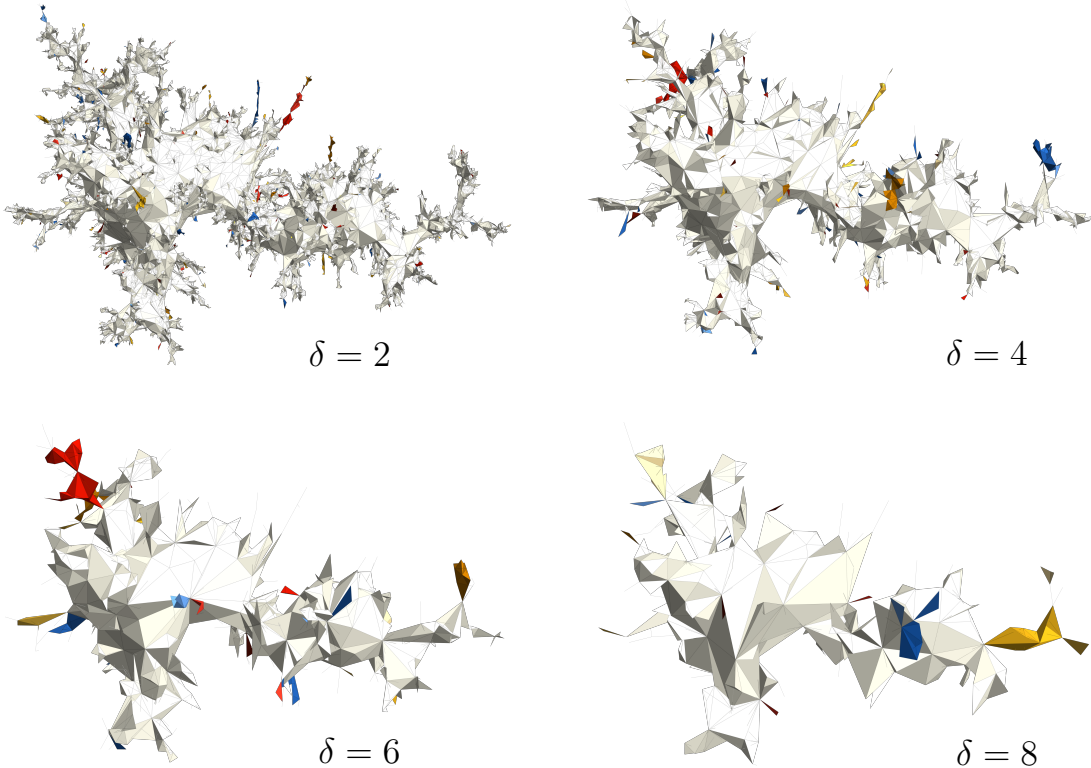


Figure 24: Coarse-grainings of the spherical EDT configuration of Fig. 19 with initial volume $N_2 = 100k$, at resolution $\delta = 2, 4, 6$ and 8 , showing a large mother universe (white) and bubbles that appear due to pinching (coloured).

a more quantitative understanding of the number and sizes of the bubbles, we present another diagrammatic representation of the same four configurations in Fig. 25. Individual spherical components or bubbles are represented by discs whose radius is proportional to $\log(\tilde{N}_2/2)$, where \tilde{N}_2 is the number of coarse-grained triangles in the bubble, which is also displayed alongside the disc. (The label for bubbles with $\tilde{N}_2 = 2$ is suppressed to avoid clutter.) A line is drawn between bubbles if they are connected by a pinching vertex or by one or more loose

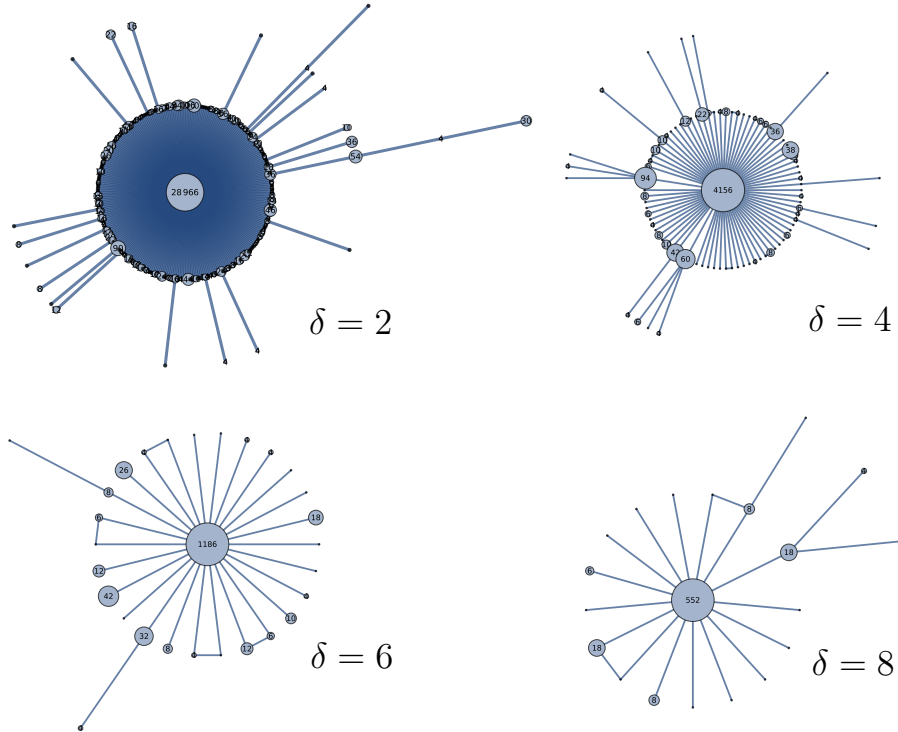


Figure 25: Bubble diagrams of the four coarse-grained Delaunay triangulations depicted in Fig. 24, with discs associated to bubbles, and bubble volumes given in terms of coarse-grained triangle units, as described in the main text.

edges in the coarse-grained triangulation T_δ .²⁷ All diagrams exhibit the presence of a mother universe at the centre, where the by far largest fraction of the volume is located, with a first generation of much smaller neighbouring bubbles, a much sparser second generation of small bubbles, and occasional instances of bubbles of a higher generation (in the examples shown, these are only present in the diagram for $\delta = 2$).

Unlike what we found in 2D Lorentzian quantum gravity, the nontrivial aspects of the effective homology in the Euclidean case are not just global, but also local²⁸, in the sense that the expectation value $\langle \beta_2(\delta) \rangle$ behaves nonclassically for all values of δ . This behaviour is related to the well-known fractal structure of 2D Euclidean quantum gravity. It can be characterized by the presence of so-called minimal-neck baby universes ("minbus"), parts of the two-dimensional geometry that are connected to a mother universe by minimal necks, consisting of closed loops of three lattice links [39, 40]. Although our construction does not exactly identify such minbus, we show in [9] that the bubble structure we find is close enough to establish (for $\delta = 2$) a quantitative relation with the string susceptibility, a scaling parameter that in these references is extracted by measuring the statistical distribution of minbu sizes. Our bubble diagrams of Fig. 25 suggest that the fractal-like, hierarchical structure of a mother universe and subsequent generations of smaller bubbles is preserved during coarse-graining, at least at a qualitative level.

²⁷Note that this leads to closed loops in the bubble diagram whenever there is a triple or higher-order meeting point between bubbles in T_δ . In Fig. 25 this happens in the diagrams for $\delta = 6$ and $\delta = 8$. It does *not* imply that T_δ itself contains noncontractible loops (which it does not).

²⁸Strictly speaking, in 2D quantum gravity without topology change there is no distinction between local and global, since any length scale is set by a cosmological constant Λ , the continuum counterpart of the coupling λ appearing in the bare actions in (8) and (11). However, in 2D CDT, by choosing suitable combinations of the two-volume N_2 and the time extension t_{tot} , we can create a "bulk regime" largely free of the effects of global winding numbers, as we have seen.

6 Conclusions and Outlook

By explicit construction, we have shown that the tool of *effective homology* can be used to characterize the quantum geometry in two-dimensional models of quantum gravity, defined nonperturbatively as continuum limits of dynamically triangulated lattice theories. The key idea is to construct a set of observables describing local metric properties of the quantum space(-time) by using the powerful machinery of TDA after applying a local coarse-graining algorithm to the path integral configurations. A coarse-graining of resolution δ produces a (generalized) triangulation with typical edge length δ (an integer in original lattice units): $\delta = 1$ reproduces the original triangulation, $\delta = 2$ results in a triangulation with edge length 2 (and correspondingly fewer triangles), and so forth. Although the original triangulations all have the same, fixed topology (of a torus in the Lorentzian and a sphere in the Euclidean case), this need not be the case after coarse-graining, since the latter by construction does not resolve substructures of linear size smaller than δ .

The concrete observables we measured on lattices of volume $N_2 \leq 400k$ were the Betti numbers $\beta_i(\delta)$, $i = 0, 1, 2$, as a function of the coarse-graining scale. The only nontrivial behaviour of their expectation values we found in the Lorentzian model comes from large δ , where the cells of the coarse-grained Voronoi decomposition become sufficiently large to completely wrap around one or both of the torus directions, leading to singular pinchings of the associated Delaunay triangulation that affect both $\langle \beta_1 \rangle$ and $\langle \beta_2 \rangle$ (Fig. 17). A similar pinching mechanism is also present in the Euclidean model, but already at a local scale, which affects the expectation value $\langle \beta_2 \rangle$ already at the smallest nontrivial coarse-graining $\delta = 2$ (Fig. 22).

Returning to the theme of symmetry we introduced in Sec. 1, since the Lorentzian and Euclidean quantum gravity models in 2D do not have nontrivial classical limits, we cannot examine the issue of *recovering* any symmetries, but we can still ask whether their quantum geometries may support continuous isometries of some kind. For the Lorentzian model, our analysis has not found any obstructions, at least not of a local kind and when staying away from length scales where global pinchings can occur. By contrast, the bubble structure of Euclidean quantum gravity presents a clear obstacle to the existence of such symmetries.

Our investigation demonstrates the feasibility of the concept of effective homology and its technical implementation, for nontrivial quantum gravity models of either spacetime signature in two dimensions. We have rediscovered the well-known fractal structure of Euclidean Liouville gravity, consisting of mother and baby universes, but otherwise have not discovered any new features. Given the well-documented and relatively straightforward properties of both the Lorentzian and Euclidean models, this was not to be expected either. However, our explicit set-up did not rely in an essential way on working in two dimensions, which opens the way to its application in four dimensions and Lorentzian signature, which is our main target and motivation.

The higher-dimensional case will be richer and inevitably more complex, with more freedom of how to handle topology changes during coarse-graining, generalizing the “pinching” that was the main feature in two dimensions. Any choices should be guided by what is expected to be important for phenomenologically interesting observables, including those related to matter coupling. Also, computational efficiency and lattice size, which hardly played a role in the current study, will become factors to be considered in $D > 2$. The 4D application will break genuinely new ground, given our current, limited understanding of its local quantum geometry [3,8] and how to characterize it in terms of suitable observables. Is it really a quantum foam on short scales, and does it support local or global symmetries when coarse-grained suitably? – We look forward to investigating the physical case of 4D Lorentzian quantum gravity in the near future.

Acknowledgments

The contribution of JvdD and RL is supported by a grant in the Open Competition ENW-M Program of the Dutch Research Council (NWO), with grant ID <https://doi.org/10.61686/IBVAP30787>. The research of MS was supported by a Radboud Excellence fellowship from Radboud University in Nijmegen, Netherlands, and by an NWO Veni grant under grant ID [<https://doi.org/10.61686/SUPEH07195>]. JvdD and RL thank the Perimeter Institute for hospitality. This research was supported in part by Perimeter Institute for Theoretical Physics. Research at Perimeter Institute is supported by the Government of Canada through the Department of Innovation, Science and Economic Development and by the Province of Ontario through the Ministry of Colleges and Universities.

Appendix A

In this appendix, we provide some details about how we construct the Voronoi decomposition of a triangulation T whose dual is a coarse-grained Delaunay triangulation T_δ of a given resolution δ . Our starting point is the original triangulation T , where each triangle of T has already been coloured and decorated according to the prescription outlined in Sec. 4.2 and illustrated in Fig. 3. We separately keep track of type-1 and type-2 triangles, to make sure that during the construction of the Voronoi decomposition every piece of boundary segment and every triple intersection of such segments has been taken into account.

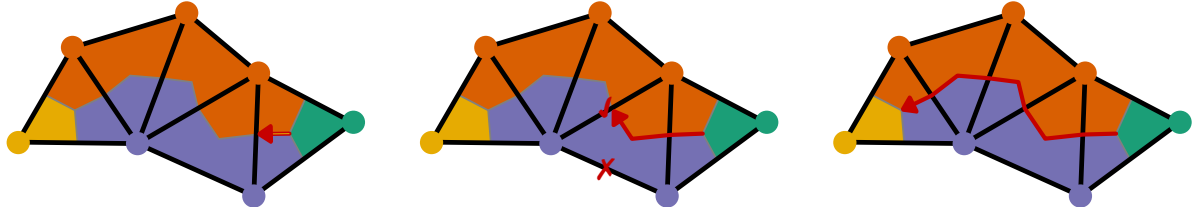


Figure 26: Moving through a sequence of triangles to identify a boundary segment between two triple points belonging to the Voronoi decomposition.

Our algorithm proceeds by considering each type-2 triangle in turn, and establishing the three nearest triple points that can be reached from the triple point at the centre of this triangle by following boundaries between differently coloured regions on the triangulation T . This determines the three boundary segments of the Voronoi decomposition meeting at the initial triple point.

The process of finding a nearest neighbour²⁹ is illustrated by Fig. 26. Starting from a triple vertex (left figure), we choose to walk along one of the three boundaries to the centre of the next triangle, in this case by crossing the triangle edge between the violet and the orange vertex of the triangle. There are then two possibilities: if the second triangle is of type 2, we have found the other triple point where the boundary segment ends; we then go back to the first triangle and explore the next direction, say, anticlockwise. If the second triangle is of type 1 (as is the case here, central figure), we next cross the triangle edge which again has a violet vertex on the left (in the direction indicated by the arrow) and an orange vertex on the right. Such an edge always exists, since the third vertex of the triangle has to be either violet or orange. We then repeat the same step by continuing to the next triangle, always crossing the triangle edge with the violet vertex on the left and the orange one on the right, until the process ends

²⁹We use a data structure where together with each triangle we store the labels of its neighbouring triangles, such that finding a neighbour is simply a look-up in constant time.

when we encounter a type-2 triangle with a triple point (right figure). Each time we traverse a type-1 triangle, we remove it from the list, to keep track of which such triangles have been visited.

In this manner we exhaust all type-2 triangles. It can then happen that not all type-1 triangles have been visited yet. They must be parts of closed boundary segments without any triple points, like the ones we met earlier in Sec. 4.3.1 and Fig. 9. One proceeds by picking such a triangle from the list of remaining type-1 triangles and following the boundary between the differently coloured regions by traversing subsequent triangles, analogous to what is shown in Fig. 26. Eventually this path must close on itself. This process is repeated until no type-1 triangles are left. In this way we guarantee that all boundaries have been visited. The result is the Voronoi decomposition, whose cells, boundary segments and triple points we associate with the dual vertices, edges and triangles respectively of the Delaunay triangulation, as described in Sec. 4.3.

Appendix B

This appendix provides some details of our procedure to adjust a Delaunay triangulation such that it provides a well-defined input to GUDHI's computation of Betti numbers, without changing its homology. This input requires that each p -simplex is given in the form of a list $\{v_0, v_1, \dots, v_p\}$ of $p + 1$ vertices. It cannot handle a situation where distinct edges share the same end points $\{u, v\}$ or distinct triangles share the same corner points $\{u, v, w\}$. Both of these cases can arise during the coarse-graining procedure of Sec. 4, as was explained there.

To eliminate these irregularities systematically, we proceed in two steps. First, we identify all vertex pairs of the Delaunay triangulation which are connected by more than one edge. For each such vertex pair $\{u, v\}$, we insert an additional vertex in the middle of all but one of the edges connecting u and v , such that there are two edges instead of one. At the same time, the triangles on either side of the edge are subdivided accordingly, such that there are four triangles instead of two, as illustrated by Fig. 27, left. (If the edge was a loose edge, there are no triangles to be subdivided.) It can in principle happen that a newly created edge is part of a loop of length two, in which case the same procedure has to be applied to it also.

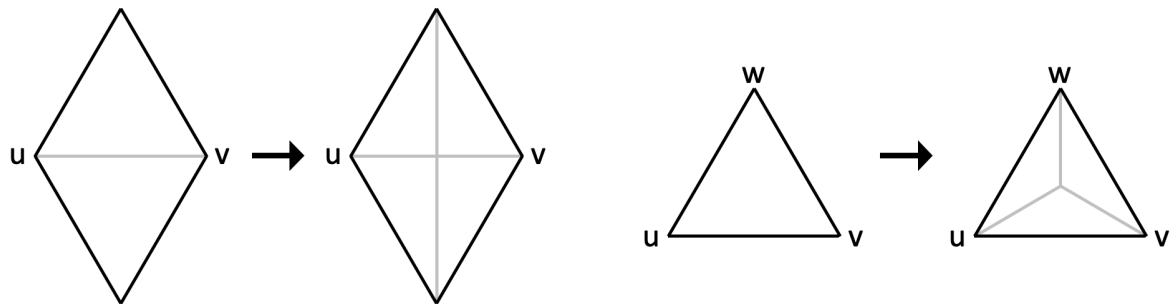


Figure 27: Removing irregularities from Delaunay triangulations: multiple edges sharing the same two vertices u and v are subdivided (left); multiple triangles sharing the same three vertices u , v and w are subdivided (right).

After all loops of length two have been eliminated, we identify all vertex triples of the Delaunay triangulation which are shared by more than one triangle. For each such triple $\{u, v, w\}$, we insert an additional vertex in the middle of all but one of the triangles with corner points u , v and w , such that there are three triangles instead of one, as illustrated by Fig. 27, right. Note that the two operations depicted here coincide with local Monte Carlo moves implemented in two-dimensional CDT and EDT respectively (see, for example, [25, 41]),

and do not change the connectivity of the triangulations. The final result is a two-dimensional simplicial complex, from which we prepare the input for GUDHI in the form of three lists:

- a list of vertices: $\{v_0, v_1, \dots, v_{N_0}\}$,
- a list of edges: $\{\{u_0, v_0\}, \{u_1, v_1\}, \dots\}$, and
- a list of triangles: $\{\{u_0, v_0, w_0\}, \{u_1, v_1, w_1\}, \dots\}$.

References

- [1] J. Ambjørn, A. Görlich, J. Jurkiewicz and R. Loll, *Nonperturbative quantum gravity*, Phys. Rep. 519 (2012) 127-210 [arXiv:1203.3591, hep-th].
- [2] R. Loll, *Quantum gravity from causal dynamical triangulations: A review*, Class. Quant. Grav. 37 (2020) 013002 [arXiv:1905.08669, hep-th].
- [3] J. Ambjørn and R. Loll, *Causal dynamical triangulations: Gateway to nonperturbative quantum gravity*, in *Encyclopedia of Mathematical Physics 2nd Edition*, eds. M. Bojowald and R.J. Szabo, Elsevier (2025) 555-567, doi: 10.1016/B978-0-323-95703-8.00109-9 [arXiv:2401.09399, hep-th].
- [4] J. Ambjørn, J. Jurkiewicz and R. Loll, *Emergence of a 4-D world from causal quantum gravity*, Phys. Rev. Lett. 93 (2004) 131301 [arXiv:hep-th/0404156, hep-th].
- [5] J. Ambjørn, A. Görlich, J. Jurkiewicz and R. Loll, *Planckian birth of the quantum de Sitter universe*, Phys. Rev. Lett. 100 (2008) 091304 [arXiv:0712.2485, hep-th].
- [6] N. Klitgaard and R. Loll, *How round is the quantum de Sitter universe?*, Eur. Phys. J. C 80 (2020) 990 [arXiv:2006.06263, hep-th].
- [7] J. Ambjørn, J. Jurkiewicz and R. Loll, *The spectral dimension of the universe is scale-dependent*, Phys. Rev. Lett. 95 (2005) 171301 [arXiv:hep-th/0505113].
- [8] R. Loll, *Nonperturbative quantum gravity, unlocked through computation*, in *Quantum Gravity and Computation*, eds. D. Rickles, X.D. Arsiwalla and H. Elshatlawy, Routledge, New York (2025) 277–294 [arXiv:2501.17972, hep-th].
- [9] J. van der Duin, R. Loll, M. Schiffer and A. Silva, *Exploring quantum spacetime with topological data analysis* [arXiv:2510.XXXXX, hep-th].
- [10] S. Carlip, *Spacetime foam: a review*, Rept. Prog. Phys. 86 (2023) 6, 066001 [arXiv:2209.14282, gr-qc].
- [11] R. Loll and A. Silva, *Measuring the homogeneity of the quantum universe*, Phys. Rev. D 107 (2023) no.8, 086013 [arXiv:2302.10256, hep-th].
- [12] J. Ambjørn, A. Görlich, J. Jurkiewicz and R. Loll, *The nonperturbative quantum de Sitter universe*, Phys. Rev. D 78 (2008) 063544, [arXiv:0807.4481, hep-th].
- [13] S. Carlip, *Dimension and dimensional reduction in quantum gravity*, Class. Quant. Grav. 34 (2017) no.19, 193001 [arXiv:1705.05417, gr-qc].
- [14] R. Loll, G. Fabiano, D. Frattulillo and F. Wagner, *Quantum gravity in 30 questions*, PoS (CORFU2021) 316 [arXiv:2206.06762, hep-th].

- [15] J. Ambjørn, J. Gizbert-Studnicki, A. Görlich and D. Németh, *Topology induced first-order phase transitions in lattice quantum gravity*, JHEP 04 (2022) 103 [arXiv:2202.07392, hep-lat].
- [16] G. Carlsson, *Topology and data*, Bull. Am. Math. Soc. 46 (2009) 255-308, doi: S0273-0979-09-01249-X.
- [17] E. Munch, *A user's guide to topological data analysis*, J. Learn. Anal. 4 (2017) 47-61, doi: 10.18608/jla.2017.42.6.
- [18] A. Hatcher, *Algebraic topology*, Cambridge University Press (2002), available at <https://pi.math.cornell.edu/~hatcher/AT/AT.pdf>
- [19] N. Otter, M.A. Porter, U. Tillmann, P. Grindrod and H.A. Harrington, *A roadmap for the computation of persistent homology*. EPJ Data Sci. 6 (2017) 17 [arXiv:1506.08903, math.AT].
- [20] T. Kawano, D. Obster and N. Sasakura, *Canonical tensor model through data analysis: Dimensions, topologies, and geometries*, Phys. Rev. D 97 (2018) 124061 [arXiv:1805.04800, hep-th].
- [21] S. Major, D. Rideout and S. Surya, *Stable homology as an indicator of manifoldlikeness in Causal Set theory*, Class. Quant. Grav. 26 (2009) 175008 [arXiv:0902.0434, gr-qc].
- [22] F. Ruehle, *Data science applications to string theory*, Phys. Rept. 839 (2020) 1-117, doi: 10.1016/j.physrep.2019.09.005.
- [23] G. Wilding, K. Nevenzeel, R. van de Weygaert, G. Vegter, P. Pranav, B.J.T. Jones, K. Efstrathiou and J. Feldbrugge, *Persistent homology of the cosmic web – I. Hierarchical topology in Λ CDM cosmologies*, Mon. Not. Roy. Astron. Soc. 507 (2021) 2968-2990 [arXiv:2011.12851, astro-ph.CO].
- [24] H. Edelsbrunner and J.L. Harer, *Computational topology: an introduction*, American Mathematical Society, Providence (2010), see also <https://www.ams.org/publications/authors/books/postpub/mbk-69>.
- [25] J. Ambjørn, M. Carfora and A. Marzuoli, *The geometry of dynamical triangulations*, Lect. Notes Phys. Monogr. 50, Springer, Berlin (1997) [arXiv:hep-th/9612069].
- [26] J. Gallier and J. Quaintance, *Aspects of convex geometry. Polyhedra, linear programming, shellings, Voronoi diagrams, Delaunay triangulations*, book in progress (2022), manuscript available at <https://www.cis.upenn.edu/~jean/gbooks/convexpoly.html>
- [27] R. Loll and T. Niestadt, *What is the curvature of 2D Euclidean quantum gravity?*, JHEP 04 (2025) 158 [arXiv:2407.18120, hep-th].
- [28] The GUDHI project, *GUDHI User and Reference Manual*, URL: <https://gudhi.inria.fr/doc/3.11.0/>
- [29] J. Henson, *Coarse graining dynamical triangulations: A new scheme*, Class. Quant. Grav. 26 (2009) 175019 [arXiv:0907.5602, gr-qc].
- [30] T. Wang, *Poisson-Disk Sampling: Theory and Applications*, In: Lee, N. (eds) Encyclopedia of Computer Graphics and Games. Springer, Cham. doi: 10.1007/978-3-319-08234-9_398-1.

- [31] D. Dunbar and G. Humphreys, *A spatial data structure for fast Poisson-disk sample generation*, ACM Trans. Graph. 25, 3 (2006), 503–508 doi: 10.1145/1141911.1141915.
- [32] M. Erwig, *The graph Voronoi diagram with applications*, Networks 36 (2000)156-163, doi: 10.1002/1097-0037(200010)36:3<156::AID-NET2>3.0.CO;2-L.
- [33] J. van der Duin, *dynamical-triangulation/dyntri-rs: First release (v0.9.0)*, Zenodo (2025), doi: 10.5281/zenodo.16950228.
- [34] J. Ambjørn and R. Loll, *Nonperturbative Lorentzian quantum gravity, causality and topology change*, Nucl. Phys. B 536 (1998) 407-434 [arXiv:hep-th/9805108].
- [35] J. van der Duin and R. Loll, *Curvature correlators in nonperturbative 2D Lorentzian quantum gravity*, Eur. Phys. J. C 84 (2024) 7, 759 [arXiv:2404.17556, hep-th].
- [36] J. van der Duin, *Curvature correlations in quantum gravity*, Master Thesis, Radboud University (2023), link: <https://surfdrive.surf.nl/files/index.php/s/dpHByvWQOD8B9GJ?path=%2FGravity>
- [37] J. Brunekreef and R. Loll, *Quantum flatness in two-dimensional quantum gravity*, Phys. Rev. D 104 (2021) no.12, 126024 [arXiv:2110.11100, hep-th].
- [38] O. Bernardi, *Bijective counting of Kreweras walks and loopless triangulations*, Journal of Combinatorial Theory, Series A **114**, 5 (2007) 931-956 [arXiv:math/0605320, math].
- [39] S. Jain and S.D. Mathur, *World sheet geometry and baby universes in 2-D quantum gravity*, Phys. Lett. B 286 (1992) 239-246 [arXiv:hep-th/9204017].
- [40] J. Ambjørn, S. Jain and G. Thorleifsson, *Baby universes in 2-d quantum gravity*, Phys. Lett. B 307 (1993) 34-39 [arXiv:hep-th/9303149].
- [41] J. Brunekreef, A. Görlich and R. Loll, *Simulating CDT quantum gravity*, Comput. Phys. Commun. 300 (2024) 109170 [arXiv:2310.16744, hep-th].